AD-A250 816

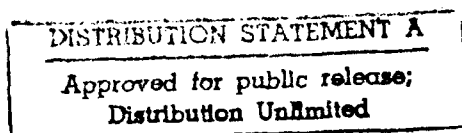# Solution of Potential Problems Using an Overdetermined Complex Boundary Integral Method

W.W. Schultz and S.W. Hong
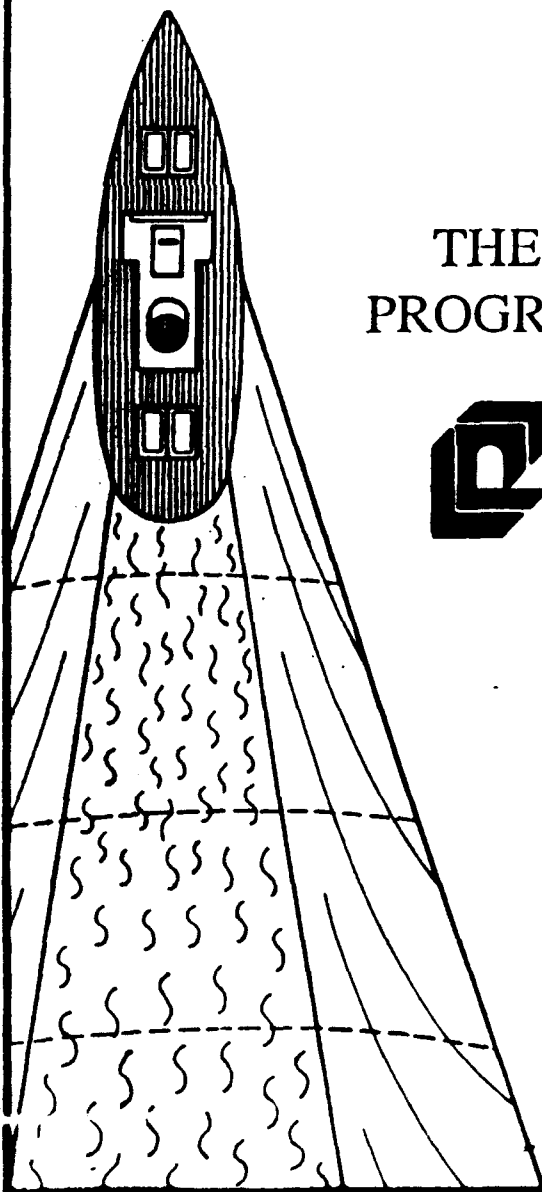Department of Mechanical Engineering and Applied Mechanics

January 20, 1988

DTIC
ELECTE
JUN 2 1992
S
C D

92-13794

92 5 26 020

# THE UNIVERSITY OF MICHIGAN
# PROGRAM IN SHIP HYDRODYNAMICS

## COLLEGE OF ENGINEERING

NAVAL ARCHITECTURE &
MARINE ENGINEERING

AEROSPACE ENGINEERING

MECHANICAL ENGINEERING &
APPLIED MECHANICS

SHIP HYDRODYNAMIC
LABORATORY

SPACE PHYSICS RESEARCH
LABORATORY

ERIM

## Abstract

The advantages of solving potential problems using an overdetermined boundary integral element method are examined. Representing a two-dimensional potential solution by an analytic complex function forms two algebraic systems from the real and imaginary parts of the discretized form of Cauchy's theorem. Depending on which boundary condition is prescribed. the real or the imaginary algebraic system is diagonally dominant. Computations show that the errors of the strong system (diagonally dominant) often have almost the same value as those of weak system (diagonally non-dominant) but with the opposite sign. The overdetermined system. composed of the combination of the real and imaginary parts, tends to average these errors, especially for circular contours. An error analysis and convergence studies for several geometries and boundary conditions are performed. A methodology for handling computational difficulties with contour corners is outlined. Further modifications are proposed and tested that show exponential convergence for smooth contours.

Accession For

| | | |
|---|---|---|
| NTIS GRA&I | ☑ | |
| DTIC TAB | ☐ | |
| Unannounced | ☐ | |
| Justification | | |

By
Distribution/
Availability Codes

| Dist | Avail and/or Special |
|---|---|
| A-1 | |

# 1 Introduction

The boundary integral method (also called the panel method) is powerful for solving potential problems. In this method, the computational domain becomes the enclosing boundary, reducing the effective dimension of the problem by one. This significantly decreases the computational effort unless the contour is highly contorted.

Boundary integral methods are usually derived from Green's theorem with an appropriate free-space Green's function. However, the solutions of two-dimensional potential problems discussed here can be described by a complex analytic function. This allows the boundary integral method to be formulated from Cauchy's integral theorem (Vinje and Brevig [1], Lai and Hromadka [2]). The elegance and simplicity of complex analysis carries over to computations as well. While the Green's function formulation and the complex method are not directly compared here, Dold and Peregrine [3], indicate that the latter method (from [1]) is clearly superior. Schultz [4] shows that the error of the complex formulation can be further reduced by solving the resulting two systems of algebraic equations in a least-squares sense for nonlinear breaking wave simulations. In this paper, we expand and formalize these ideas for model potential problems.

In general, an integral equation is solved by a numerical model that assumes the boundary is composed of piecewise-polynomial curves (panels) and the known and unknown boundary values are approximated as piecewise-continuous functions along the boundary. The truncation error in solving an integral equation is determined by the approximations of the boundary shape and the known and unknown function values on the boundary. A rather extensive error analysis of the conventional boundary integral method for a two-dimensional Neumann problem is given by Hess [5]. He shows that using parabolically-shaped elements with linearly varying singularity improves the accuracy when the effects of local element curvature are greater than that of the function derivatives. Unlike the Green's function formulations, the complex method does not depend

4

on the shape of the contour between nodes. Most complex variable boundary integral methods adopt piecewise-linear representations of the complex functions. This linear interpolation results in second-order accurate integration and typically gives second-order accurate solutions for the boundary integral solution as well.

The accuracy of the numerical solution is affected by the contour shapes, boundary conditions and nodal spacings as well as the possible singular behavior of the resulting solutions. Moran [6] shows poor convergence for a sharp-angled contour (such as airfoils) even when the solution there is smooth. In addition, singularities usually occur at an abrupt change in boundary conditions or at boundary corners [12]. The solution accuracy then further degrades unless special precautions are taken such as supplementing the piecewise-linear representations with singular functions [7].

In this paper, the error is analyzed for the complex variable boundary integral method using elements with linearly varying functions. The advantages of solving both sets (real and imaginary) of algebraic equations together in a least-squares sense are discussed. The integration error analysis shows the correlation between solution error and factors such as geometric curvature, nodal spacing, and local solution gradients. We also present further modifications in sections 6 and 7 that show exponential convergence for smooth contours.

# 2    Cauchy Boundary Integral Formulation

Cauchy's theorem is used to derive an integral equation in terms of the complex potential. The complex potential, $\beta$, is analytic inside the computational domain, $R$, and is given by

$$\beta(z) = \phi + i\psi \,, \tag{1}$$

where the two-dimensional spatial representation is given by $z = x + iy$, and $\phi$ and $\psi$ are real functions that can be identified as the velocity potential and stream function, respectively, for ideal fluid flow problems.

Figure 1 shows the problem domain and bounding surfaces. Cauchy's theorem gives

$$\oint_{\partial R} \frac{\beta(z)}{z - \zeta_k} dz = i\alpha\beta(\zeta_k) \,. \tag{2}$$

where $\alpha$ is 0 or $2\pi$ if the location of the kernel singularity, $\zeta_k$, is outside or inside the boundary, respectively. If the kernel singularity is on the boundary ($\zeta_k \in \partial R$), $\alpha$ is equal to the included angle and the integral is treated as principal-valued. For most of our computations, we take $\zeta_k$ to approach the boundary from outside of the domain so that $\alpha$ is zero. The algebraic system is formed by discretizing the integral as explained in section 3 and letting the kernel singularity approach each of the N nodal points, $\zeta_k \to z_k$. A special limiting process is then needed to evaluate the integration near $\zeta_k$.

The boundary contour $\partial R$ is composed of $\partial R_\phi$ and $\partial R_\psi$, where $\phi$ is given on $\partial R_\phi$ and $\psi$ is given on $\partial R_\psi$. For the problem to be well-posed, either $\phi$ or $\psi$ must be specified along the entire boundary. This is related to the Dirichlet or Neumann problem, respectively, in the standard formulation. Although generalized (Robin) boundary conditions can be included in these computational schemes, we do not study them here. Hence, the boundary can be categorized as the following two types:

$$Re\{\beta\} = \phi \text{ is given on } \partial R_\phi \tag{3}$$

$$Im\{\beta\} = \psi \text{ is given on } \partial R_\psi \ . \tag{4}$$

When the boundary condition is given exclusively as either $\phi$ or $\psi$ along the entire boundary, the solution is not unique, since an additional real or imaginary constant can be added to the solution. This is related to a solvability condition for the Neumann problem. Therefore, an appropriate additional condition or a replacement condition (if the problem is not to be overdetermined) is required. We have found that replacing the boundary condition at one point (i.e., assuming $\phi$ is known at every point except one, where $\psi$ is known) yields much less accurate results. Therefore, we use an additional condition, and hence, all algebraic systems are overdetermined, although sometimes only by one extra equation.

To examine the corresponding singularity system in the standard formulation. the integrand in (2) can be rewritten as

$$\frac{\phi e^{i\theta}}{z - \zeta_k} ds + i \frac{\psi e^{i\theta}}{z - \zeta_k} ds \ ,$$

where $\theta$ is the tangent angle of the boundary with the positive x axis. Hence, the contribution from the above differential element to the complex potential inside the domain is given by

$$d\beta(\zeta_k) = \frac{1}{2\pi} \left[ \frac{\phi(-i)e^{i\theta}}{z - \zeta_k} ds + \frac{\psi e^{i\theta}}{z - \zeta_k} ds \right] . \tag{5}$$

This relation shows that the integral equation (2) is equivalent to a system of distributed normal dipoles of strength $\phi$ and tangential dipoles of strength $\psi$ on the boundary. However, we can represent the potential field by using only one of the dipole systems, following the concepts of the indirect boundary integral method. (In the indirect method [16], the computational unknowns are the strengths of the distributed singularities rather than the original solution, as in the direct method.) Baker et al. [8] shows that dipole distributions are more stable than source or vortex distributions for nonlinear breaking wave simulations. We could formulate a complex integral method similar to a combination of the sources and vortices by introducing, for example, a logarithmic singularity into (2) rather than the simple pole. However, our preliminary numerical studies indicate that the simple pole in (2) performs better than other singularities.

7

including those of higher-order.

# 3  Numerical Model

Following the procedure of Vinje and Brevig [4], both the boundary contour and the complex potential are represented as piecewise-linear functions. The location and complex potential at the $j^{th}$ node point are given by $z_j$ and $\beta_j$, respectively. Then $\beta$ on $j^{th}$ panel is described by

$$\beta = \frac{1}{z_{j+1} - z_j} \left[ \beta_j(z_{j+1} - z) + \beta_{j+1}(z - z_j) \right] . \tag{6}$$

We can choose $\zeta_k$ of Eq. (2) to be anywhere, although since we treat the case $\alpha = 0$, it must be outside the solution domain. Typically, it is chosen to approach some point on the $k^{th}$ panel. The panel midpoint and the node point are favored equally for $\zeta_k$ in previous formulations. Our studies show no significant differences in accuracy and convergence rates between those two cases. Hence, we choose the endpoints, which are easier to code. We also have studied a more overconstrained problem by placing control points at the node points *and* the midpoints and have found no significant improvement. In section 9 we examine the advantages of moving $\zeta_k$ away from the contour.

Letting $\zeta_k$ approach each node from the outside yields the algebraic equivalent of (2) approximated as [1]

$$\sum_{j=1}^{N} \beta_j \Gamma_{jk} = 0 \qquad \text{for } k = 1, \ldots, N \tag{7}$$

where

$$\Gamma_{jk} = \frac{z_{j+1} - \zeta_k}{z_{j+1} - z_j} \ln\left(\frac{z_{j+1} - \zeta_k}{z_j - \zeta_k}\right) - \frac{z_{j-1} - \zeta_k}{z_j - z_{j-1}} \ln\left(\frac{z_j - \zeta_k}{z_{j-1} - \zeta_k}\right) \text{ for } j \neq k, \tag{8}$$

$$\Gamma_{kk} = \ln\left(\frac{z_{k+1} - z_k}{z_{k-1} - z_k}\right) . \tag{9}$$

Eq. (8) is evaluated using L'Hospital's rule when $j = k + 1$ or $k - 1$. Moving the unknown boundary conditions to the right-hand side gives the following complex algebraic system for

8

unknown $\phi_j$ or $\psi_j$:

$$\sum_{j \in \partial R_\psi} \Gamma_{jk} \phi_j + i \sum_{j \in \partial R_\phi} \Gamma_{jk} \psi_j = - \sum_{j \in \partial R_\phi} \Gamma_{jk} \phi_j - i \sum_{j \in \partial R_\psi} \Gamma_{jk} \psi_j, \text{ for } k = 1, \ldots, N. \quad (10)$$

$\Gamma_{jk}$ represents the influence of the $k^{th}$ node kernel singularity on the $j^{th}$ node complex potential $3_j$. In general, $\Gamma_{k-1,k}$, $\Gamma_{kk}$, and $\Gamma_{k+1,k}$ have the dominant influence on the $k^{th}$ equation except for contours that are not convex or have sharp cusps. The imaginary part of $\Gamma_{kk}$ is nearly $-\pi$ and the real part is nearly zero for uniformly-spaced nodes on smooth parts of the contour, and exactly $-\pi$ and zero, respectively, for flat contours. On the other hand, the imaginary parts of $\Gamma_{k-1,k}$ and $\Gamma_{k+1,k}$ are nearly zero while the real parts are not small.

Choosing the imaginary part of system (8) for the $k^{th}$ equation where $\psi$ is given and the real part where $\phi$ is given, results in a system matrix with a strong diagonal. Taking the other systems results in a system matrix with a weak diagonal. We now refer to the former system as the *strong* system and the latter as the *weak* system. The strong system is very similar to a Fredholm integral equation of the second kind, and the weak system is similar to a Fredholm integral equation of the first kind. As indicated in the introduction, we solve the weak and strong systems together as an *overdetermined* system in a least-squares sense and compare these results to those obtained from the individual systems.

# 4 Truncation Error in Numerical Integration

The truncation error in the numerical integration is analyzed for the case of uniformly-spaced nodes. In general, the dominant truncation error in (2) for the $k^{th}$ control point occurs in the integration from $z = z_{k-1}$ to $z = z_{k+1}$, as shown in Figure 1. Rewriting the integral (2) as

$$I_k = \int_{z_{k-1}}^{z_{k+1}} \frac{\beta(z)}{z - \zeta_k} dz \ . \tag{11}$$

For uniformly-spaced nodes with slowly varying geometric curvature, we can examine the integral $I_k$ by expanding $\beta(z)$ at $z = \zeta_k$ as,

$$\beta(z) = \beta(\zeta_k) + \beta'(\zeta_k)(z - \zeta_k) + \frac{1}{2}\beta''(\zeta_k)(z - \zeta_k)^2 + O(\|z - \zeta_k\|^3) \ . \tag{12}$$

Using (12), we can write Eq. (11) as

$$I_k = I_k^{(0)} + I_k^{(1)} + I_k^{(2)} + O(\|z - \zeta_k\|^3) \ , \tag{13}$$

where

$$I_k^{(0)} \quad \beta(\zeta_k) \ln\left(\frac{z_{k+1} - z_k}{z_{k-1} - z_k}\right), \tag{14}$$

$$I_k^{(1)} = \beta'(\zeta_k)(z_{k+1} - z_{k-1}), \tag{15}$$

and

$$I_k^{(2)} = \frac{1}{4}\beta''(\zeta_k)[(z_{k+1} - z_k)^2 - (z_{k-1} - z_k)^2] \ . \tag{16}$$

Since our numerical model assumes $\beta$ varies linearly between nodes. the dominant truncation error in the calculation of $I_k$ is $I_k^{(2)}$.

When $\beta$ is linear, the integration is exact and the integral equation algorithm gives exact solutions. In Figure 2, a very strong correlation between $Re\{I_k^{(2)}\}$ and the solution error is shown for a problem inside a circular contour with uniformly-spaced nodes when $\phi$ is given as $Re\{\sin z\}$. The correlations are nearly 1.0 and -1.0 for the weak and strong systems, respectively. Figure 3a shows that the strong and weak systems give approximately the same errors but of opposite

sign. The error distribution along the same contour for another test function, in which $\beta = e^{-iz}$, is shown in Figure 3b. The results for a problem when the solution domain is outside the unit circle are given in Figure 3c. This example represents a dipole in a uniform potential gradient. The imaginary part of the potential should be zero on the unit circle. To solve this problem. the uniform part must be subtracted out so that there is no contribution from the contour at infinity. A branch cut is chosen to connect the contour at infinity to the inside circular contour. which is then integrated in a clockwise sense. All examples in Figure 3 show the typical error cancellation characteristics of the overdetermined system. The overdetermined system averages the errors of weak and strong systems so that the error distribution curves of the overdetermined system nearly collapse to the abscissa. Other calculations show that this error cancellation for the outer problem is nearly complete when the dipole is moved from the origin but still well inside the contour.

It is noteworthy that the solutions of the weak system sometimes show small oscillations with wavelengths twice the nodal spacing. This common *zig-zag* instability is due, in part, to the nearly singular matrix. At times, when this numerical instability becomes large, the weak system matrix becomes so numerically singular that direct inversion is no longer possible. Then iterative refinement. as done here. is required.

For noncircular contours, the errors contributed from off-diagonal elements grow as the local geometric curvature increases. Figure 4 shows the error distribution curve and the correlation between error and $Re\{I_k^{(2)}\}$ when $\varphi$ is given for an elliptical contour with an eccentricity of 0.9165 (the major axis of unit radius for the examples shown here is always centered on the x-axis). A relatively strong correlation still exists, but the error of the weak system is more sensitive near zero $I_k^{(2)}$. In this case, the cancellation characteristic of the overdetermined system is no longer nearly perfect. as shown in Figure 3. Table I shows the correlation numbers between the solution error and $Re\{I_k^{(2)}\}$ for various ellipses with eccentricities of 0.0 to 0.9798 (minor axes in the y

11

direction of 1 to 0.1). The weak system loses its strong correlation at an eccentricity of 0.9798, where large, spurious oscillatory behavior develops in the solution.

We will show that the error cancellation of the overdetermined system seems more dependent on the variation of geometric curvature and on the nodal spacing, rather than on the solution characteristics.

# 5 Numerical Investigation

Comparisons of accuracy, convergence rate, and computing time are made for weak. strong, and overdetermined sets of system (10). The effects of nonuniform nodal spacing, types of boundary conditions, nearly singular solution characteristics, and contour shape on the solution errors are also investigated.

The overdetermined matrix problem can be solved two ways. One method uses a routine based on the Householders transformation [9]. This routine takes an order of $U^2$ V operations, where U is the number of unknowns and V is the number of equations. The other uses a conjugate gradient iterative technique [10], which solves the problem in an order of UVL operations. where L is the number of iterations. The computational savings of the iterative technique would be important if time marching were desired. especially since a good initial guess is available from the previous time step. However, even with a homogeneous initial guess. a typical solution for a nonsingular matrix requires less than 10 iterations.

The iterative solver often takes more computing time than the Householders transformation method for the weak system, but iterative methods are more reliable when the system is nearly singular. as is true in the weak system. Here, we always use the conjugate gradient iterative method with a zero initial iterate to compare the efficiency of the three systems.

## 5.1 Rate of Convergence and Computing Time

The root mean square errors ($E_2$) and corresponding computing times are examined as a function of the number of nodes to determine convergence rates and computational efficiency. The maximum errors ($E_\infty$) follow a very similar pattern and hence are not shown. Figure 5 shows $E_2$ for the three systems in log-log scale with uniformly-spaced nodes on a circular contour when $\phi$ is given as $Re\{\sin z\}$. Single-precision (six digits) results are limited to approximately five decimal point accuracy as round-off error dominates truncation error beyond N=32. The

13

overdetermined system is more accurate by one digit at $N = 16$, and the convergence rate of the overdetermined system is twice that of the weak or strong systems.

In Figure 6, computing times of the single-precision program are shown. For the same N, the computing time of the overdetermined system is the largest and the computing time to solve the weak system increases rapidly when $N > 32$ as the system matrix becomes more singular and the number of iterations increases. Figure 6 clearly shows that the overdetermined solution is the most efficient of the three systems for this example.

The effect of the contour shape on the efficiency of inner problems is examined for elliptical contours with various eccentricities ($e = 0.0$ to $0.995$) for the same $\beta$. The diameter of the major axis is fixed to be 2.0 and centered on the x axis. As the eccentricity increases, the $E_2$ of the overdetermined system increase. but those of the strong systems decrease, as shown in Figure 7. The $E_2$ of the weak system for $e \geq 0.9165$ increase due to the more oscillatory behavior of the solution. In Table II, the $E_2$ are given as a function of the number of nodes for various ellipses. In most cases, the overdetermined system gives the best results, except for highly eccentric elliptical contours where the weak system's oscillations affect the overdetermined solution as well.

The $E_2$ convergence rates determined at the largest computed N are compared in Table II for inner problems for ellipses with various eccentricity. Astonishingly, the convergence rate of the overdetermined system for a circular contour ($e = 0$) approaches 4.0. The convergence rates of all the other examples are the predicted 2.0.

$E_2$ for outer problems, when $\beta = 1/z$, are also calculated and given in Table III for various ellipses ($0 \leq e \leq 0.995$) with a double-precision program. The results of the overdetermined system are the best for all cases tested. The convergence rates approach 2.0 for the weak and strong systems. The convergence rates of the overdetermined system also approach 2.0 except at $e = 0$,

14

which again exhibits fourth-order convergence. We also have obtained fourth-order accuracy for exterior problems when the simple poles are placed in the interior, not close to the boundary. As the eccentricity increases, $E_2$ increases for all systems due to the more rapid variation of the function and the kernel.

Since our numerical model uses a piecewise-linear representation for the potential function, we expect second-order convergence. However, for some cases, the convergence rates of the overdetermined system approach fourth-order due to the cancellation of errors between the weak and the strong systems. Our examples show that these cancellations occur when the contour is circular (or nearly so) with uniformly-spaced nodes. Some calculations not described here have shown third- and sixth-order convergence for the strong and overdetermined systems, respectively, when a cubic-spline representation is used for $\beta$.

## 5.2 Nonuniform Nodal Spacing

Sometimes nonuniform nodal spacing is desirable when solution refinement is needed due to large solution gradients. Also, the nodal spacing in problems with convective nodes (such as free surface flow problems) becomes nonuniform. This can cause numerical instabilities, so that a filtering scheme or a regridding scheme is needed to maintain uniform spacing [11].

In Figure 8, a schematic of nonuniformly-spaced nodes is shown. The nonuniformity at node k (in an otherwise uniformly-spaced grid) is defined as the ratio between $L_e$ and $L_0$. In this case, the real part of $\Gamma_{kk}$ is no longer small. Moreover, the dominant off-diagonal terms $\Gamma_{k-1,k}$ and $\Gamma_{k+1,k}$ also change significantly while the imaginary part of $\Gamma_{kk}$ remains around $-\pi$. Hence, the local nonuniformity greatly affects the global solution characteristics.

Figure 9 shows the same example as in Figure 3a, except that node 1 is moved to form various

nonuniformities as defined by Figure 8. The errors of the strong system are affected only near that nonuniformly-spaced node. As the nonuniformity increases, the solution of the weak system deteriorates globally due to the zig-zag instability. However, if a numerical filter were used to eliminate oscillations with wavelengths equal to the node spacing, the weak system error is then comparable with the strong system and again of opposite sign. This is why the solution for the overdetermined system remains very good. Note that the error curve of the overdetermined system cannot be distinguished from the zero axis except near the moved node.

The correlation between $I_k^{(2)}$ and the solution error is still strong for strong systems, except around the $k^{th}$ node, but it is very poor for the weak system. The computing time for the weak system increases rapidly as the nonuniformity increases, since the number of iterations grows rapidly as the matrix becomes more numerically singular.

## 5.3  Types of Boundary Condition

When the boundary contour is composed of both $\partial R_\phi$ and $\partial R_\psi$, the intersecting node can present a difficulty even without any geometric discontinuity. We could expect the solution to be singular at the intersecting node. We also would usually expect that the change in boundary conditions to occur at a corner in the boundary contour (which brings other difficulties that will be discussed in section 5.5). We do not consider either case here.

We examine a circular contour with $\phi$ given on the upper half ($y > 0$) and $\psi$ on the lower half. Figure 10 shows the error distribution curves for two cases when $\beta = e^{-is}$. Either $\phi$ or $\psi$, or both can be treated as known at the intersecting nodes ($y = 0$). Only one boundary condition is prescribed at each node in (A), while both $\phi$ and $\psi$ are given at the intersecting nodes in (B). In both cases, the error of the overdetermined system is much smaller while the weak system solution again shows oscillatory behavior.

$E_2$ for these two cases are compared in Figure 11. The solutions when the additional known boundary constraints are used are better for all three systems. Convergence rates remain the same and the improvement in accuracy is small. There is also no large local error at the intersection point. We conclude that the change in boundary condition type by itself is not difficult to handle computationally.

## 5.4  Singularity Near Contour

When the boundary condition values change abruptly due to nearby singularities. the solution error at nodes near those singularities is expected to increase. As an example, the error for a unit radius circular contour where the solution has a simple pole near the contour is examined. i.e, $o$ is given as the real part of

$$\beta = \frac{1}{z - (1 + \epsilon)} ,$$

where $\epsilon$ is a small constant. The solution errors for $\psi$ of the strong system increase mainly at those nearby nodes, while those of the weak system exhibit an oscillatory behavior with peaks at nearby nodes, as shown in Figure 12. As $\epsilon$ increases, the oscillation amplitude diminishes and the weak system finally recovers the same error pattern as the strong system, but again of opposite sign.

$E_2$ shown in Figure 13 show the advantage of the overdetermined system in accuracy and convergence rate. The convergence rate for the overdetermined system is again 4.0 and those of the other systems are around 2.0. For this function, the nodal spacing must be less than $\epsilon$ before the high convergence rate is achieved. We note that the weak system is unstable due to an abrupt change in $I_k^{(2)}$, which again implies that the system matrix of the weak system is nearly singular.

## 5.5 Contours with Corners

The boundary integral accuracy is known to deteriorate in the vicinity of contour corners due to high geometric curvature. Moreover, the solution is usually singular at corners. Grisvard [12] has the most mathematically complete discussion of numerical singularities arising from the nonsmooth domain for elliptic boundary value problems. Pina, Fernandes, and Brebbia [13] suggest using mesh refinements to overcome the difficulties of nonoptimal convergence arising from an irregular boundary contour. These refinements become more important if the solution is known to be singular or to vary rapidly at a corner (Lin, Newman and Yue [14]). The numerical model can be truly singular if a modified variable is formed by subtracting out the local singular solutions from the original variable (Kelmanson [7]). Mesh refinements near corner can create difficulties with numerical instability such as at the free surface of the wave-maker problem [11].

Even if the solution is not singular at a corner, error is induced in large part by the contribution from the abrupt change in the geometric curvature. This can be seen in Eq. (16) for $I_k^{(2)}$. At a corner, the term $(z_{k+1} - \zeta_k)^2 - (z_{k-1} - \zeta_k)^2$ is not small. If $\beta''(\zeta_k)$ is nonzero at the corner, the error in numerical integration will be much larger there. In this case, the error has its maximum near the corner and can spread to the entire contour.

A modified circular contour with a corner (Figure 14) is used to test the effects of the corner on the solution accuracy. In this case, the imaginary part of $\Gamma_{kk}$ at the corner stays at $-\pi/2$ as the number of nodes increases. However, the off-diagonal influence coefficients are strongly affected by the corner and any refinement there.

As Figure 15a shows, the error of the strong system is concentrated at the corner while it remains at the previous error levels on the smooth part of the contour, as shown in Figure 3a. The error of the weak system solution oscillates over the entire contour, and the computing time (the number of iterations) increases rapidly due to the corner. However, if a numerical filter

were used to eliminate oscillations with wavelengths equal to the node spacing, the weak system would actually have smaller error than the strong system. The solution of the overdetermined system is still significantly better, but the maximum error is one thousand times greater than the solution of the overdetermined system for the smooth contour, shown in Figure 3a. All three approaches show second-order convergence for contours with corners.

The given solution for this example is analytic at the corner, but we still have very grave computational difficulties there. To make $I_k^{(2)}$ smaller, we develop a modified complex potential defined by

$$\beta_c(z) \;=\; \beta \;-\; \frac{1}{2}(z - \xi_c)^2 \beta''(\xi_c), \tag{17}$$

where $\xi_c$ is the coordinate of the corner. Thus, the second derivative of the modified complex potential $\beta_c$ is forced to be zero at the corner. This eliminates the highest-order error term in our piecewise-linear integration routine (Eq. 16) at the corner.

Figure 15b shows improved results using this modification, especially at the corner. All six solutions (weak, strong, and overdetermined systems for both the modified and unmodifed formulations) still appear to be second-order convergent for contours with corners. However, the $E_2$ or $E_\infty$ for fixed $N$ is significantly improved by the modified method. For this example, with $N = 64$, these errors are reduced by a factor of 50.

These results suggest using an iterative method for more accurate solutions to *nontest* problems, when the *unknown* value of $\beta''(\xi_c)$ is updated to a more correct value. Further developments of this method are required for problems having more than one corner and for the outer problems. It is also expected that even more accurate solutions can be obtained by requiring the higher derivatives of the modified complex potential to be zero at corners.

# 6   Desingularization

Patterson and Sheikh [15] introduce a regular boundary integral method by moving the singularity of the fundamental solution away from the boundary contour. Their rationale for doing this appears to be chiefly for desingularizing the kernel. Hence. all integrals can be computed numerically. They also claim the method "tolerates higher-order singularities" and base these conclusions on comparisons with finite element methods for elastostatic problems.

We show here that moving $z_k$ in Eq. (2) well outside the boundary has several advantages over the standard approach. While we do not perform the integrals by simple quadrature (we still use Eq. (8)), it is clear that numerical integration would no longer seriously affect the results. The determination of the influence coefficients is still simpler, since special cases are not required (as when integration passes through a singular point of the kernel). Now. however. we must decide where to locate the kernel singularities.

We use two strategies for locating the kernel singularities outside the contour shown in Figure 16. The first strategy uses the perpendicular bisector of the straight contour between adjacent nodes. This strategy has two potential difficulties. If $f$ is too small, the singular point may lie inside an actual convex-curved contour. If $f$ is too large, the singular point may lie inside the domain of a highly contorted contour. The second strategy places all singular points on a circle whose center is roughly at the centroid of the contour. This strategy avoids the difficulties of the first, but it may not place the kernel singularities sufficiently close to the contour to capture nearly singular behavior of the solution. The second strategy also has the freedom of piacing any number of kernel singularities on the circle, and hence, the algebraic system can become more or less overdetermined.

Figure 17 shows the error computed using the first strategy and two values of $f$; in this

case the nodes are placed evenly on a circular contour with $\beta = \sin z$. Here, we see that the convergence is exponential and that the overdetermined system is again the best. Figure 17 indicates that placing the singularities further from the contour is preferable. Figure 18 shows this to be the case for the same example with fixed $N = 16$. However. a price is paid in that the algebraic system becomes less diagonally dominant as $f$ increases. requiring more iterations and a tighter tolerance on the convergence parameter to achieve the acquired accuracy. For this contour we note that when $f < (1 - \cos\frac{\pi}{N})/\sin\frac{\pi}{N} \approx 0.05$ for $N = 16$, the singular point actually moves inside the contour. Figure 18 shows this happens without greatly changing the error.

Figure 19 also shows exponential convergence for the circular contour when there is a solution singularity outside the domain. In this case. a semi-log plot indicates the true exponential character of the convergence. (Only the overdetermined results are shown.) The nodal spacing must be small compared to $\epsilon$ for exponential convergence to be achieved. As a result, the convergence when $\epsilon = 0.1$ (not shown) is very poor all the way to $N = 64$. As might be expected, the most accurate solutions are no longer obtained when $f$ is large, since placing the kernel singularities further away cannot capture the effect of solution singularities close to the contour.

Although the overdetermined system still has smaller errors, it is not significantly smaller than the errors for the desingularized version of the strong or weak system (Figure 13). Similarly, Figure 20 shows that the same is true for elliptical contours. As before, all systems have second-order convergence, but the overdetermined system is slightly more accurate than the strong or weak system. (The weak system is not shown since its results are very similar to the strong system.) While desingularization greatly improves the accuracy of the weak and strong system, it only slightly improves the accuracy of the overdetermined system.

For the examples in Figures 17-20, the desingularized method is better than the method of Vinje and Brevig. However, both strategies for placing the kernel singularities off the contour do

not yield as accurate results when the contour has a corner. The convergence rate is still the same and the absolute errors increase slightly (not shown, but typically 25 percent). Further work is required to determine how to place the singular points next to the contour corners; however, our computations show that decreasing $f$ or $R_s$ near the corners is not beneficial, even when no solution singularity exists there.

The second strategy shown in Figure 16 allows an arbitrary number of kernel singularities to be used in formulating the algebraic system. When the real and imaginary systems are used, the number of singular points, $N_s$, can be less than the number of nodes, $N$, actually $N_s \geq N/2$. Table IV shows typical error results using variable $N_s$. All results are for a unit circle contour, $N = 16$, and $\beta = \sin z$, with $N_s$ singular points equally spaced on $R_s = 1.5$. Table IV shows that $N_s$ can be reduced below $N$; increasing $N_s$ further increases the accuracy insignificantly. However, increasing $N_s$ for the strong equations to overconstrain the system can be beneficial if $N_s$ is twice $N$. Table IV does not show that overdetermining the algebraic system in this manner is more expensive: more logarithms must be computed to form the influence the matrix and the resulting system is not as diagonally dominant (i.e., more iterations are required to solve the algebraic system).

# 7 Spectral methods

Following the method of Baker [17], exponential convergence can also be achieved by integrating the principal-valued form of (2) using the trapezoidal rule. To obtain this convergence, the integral must be periodic and integrated with respect to a real variable, in this case, an arclength parameter. The singular part of the integral is avoided by evaluating the integrand at every other point. The integral then becomes

$$\oint \frac{\beta(s)}{z(s) - \zeta_k} \frac{dz}{ds} ds = i\alpha\beta(\zeta_k) . \tag{18}$$

Baker indicates this expression will give exponentially convergent results if the shape (and hence $dz/ds$) is known exactly. However, in contour dynamics problems, for example, the shape is not known precisely. This problem can be overcome if the contour is known to be smooth, since $z(s)$ and hence $dz/ds$ can then be determined with exponential accuracy using spectral methods. We have performed these calculations using a standard fast Fourier transform routine (FFT) for both $x(s)$ and $y(s)$ to obtain exponential accuracy for fully nonlinear gravity waves. These results will be reported elsewhere. Here, we present results for circles, ellipses, and squares, where the shape is represented by the same Fourier representation. For the elliptical contours, the nodes are placed at constant polar angle intervals as measured from the center of the ellipse. Then the FFT is exact and the convergence is exponential, with the highest convergence for nearly circular contours, as shown in Figure 21 for $\beta = \sin z$. The overdetermined system results are nearly the same as the other systems and hence only one is shown.

A simple problem where the FFT is not exact is given using the same example of the ellipse ($e = 0.866$) with nonuniform nodal spacing. Figure 22 shows the convergence for the case when the $N^{th}$ node is moved by $\theta = .002\pi/N$. Even for this nearly imperceptible movement, the asymptotic convergence for all three systems is first order. The overdetermined system yields slightly better $E_2$. The error distribution curves for the three systems are shown in Figure 23 for $N = 32$. While $E_2$ is nearly the same for all systems, the maximum error ($E_\infty$) for the overdetermined system is significantly lower. All three systems show an oscillatory error with the wavelength on the order of the nodal spacing. This could give rise to the zig-zag instability found in many contour dynamics computations [8]. The oscillatory error of the overdetermined solution looks sufficiently regular, such that a simple filter may recover exponential convergence.

Finally, we show the convergence of the trapezoidal method in Figure 24 for a square contour centered about the origin with each side of length two, for $\beta = \sin z$. We see in this case that the convergence rate is much less than first order, with the overdetermined system giving the

best results. Unlike the previous example, no simple filter would improve the results. Part of the reason for the poor convergence is the poor convergence of $d\zeta/ds$ by the FFT due to the squares nonsmooth contour. Even when an exact $d\zeta/ds$ is used (by central difference), the convergence (although better) is still less than first order due to the discontinuities in $d\zeta/ds$ at the corner nodes. Any hope of recovering exponential convergence lies in moving all nodes by one-half the nodal spacing to avoid placing nodes at the corners.

It should be noted that the condition of the matrix obtained in this manner is excellent, and half of the coefficients are zero. This means that the algebraic solver saves computational effort. in addition to the time saved by not requiring the evaluation of logarithms. The additional time to compute the FFT's is not significant.

Obviously, more algorithm development is needed for contours with corners. In addition. it is not entirely clear how to extend this approach to domains with contours that are not simply connected.

# 8   Conclusions

Error analysis of complex variable boundary integral methods is made by truncation error analysis and numerical investigation. The overdetermined system is the most efficient and accurate in almost all cases; this sytem averages errors of the opposite sign for the solutions of the strong and weak systems. The overdetermined system has a fourth-order convergence rate for circular contours, while the other systems exhibit second-order convergence. When the contour is not circular, the convergence for all three systems is second order, but the overdetermined system is significantly more accurate for moderate $N$. All systems have difficulties at contour corners. which can be alleviated by introducing a modified complex potential such that the derivatives are zero at the corner. The overdetermined system takes the fewest number of iterations in our conjugate gradient iteration procedure. As a result, the computational time is less than twice

24

that of the weak or strong system. The increased accuracy of this method more than repays this additional cost.

For smooth contours, exponential convergence can be achieved by desingularization of the kernel or by using a trapezoidal integration rule. The exponential convergence is destroyed for noncircular contours when desingularization is used or when nodes are unevenly placed for either method. The spectral, trapezoidal method is much more accurate if the nodes are precisely placed. However, small errors can render the convergence for the trapezoidal method to be first-order. while the desingularization method is more robust. Both of these modifications perform poorly when a contour corner is present. The overdetermined system is. for the most part. the most efficient for these modifications as well.

The same approach may be extended to three-dimensional potential problems by using two sets of integral equations, one of which is derived from Green's theorem and the other from the normal derivative of Green's theorem. Hence, the advantages of solving an overdetermined system may yield greater efficiency and accuracy for three-dimensional problems as well.

# Acknowledgements

# References

1. T. Vinje and P. Brevig, *Proceedings of 3rd Int. Conf. on Numerical Ship Hydrodynamics.* Paris (1981).

2. C. Lai and T.V. Hromadka II, *Proceedings of ASCE Hydraulic Division Specialty Conference*, Orlando, Florida (1985).

3. J.W. Dold and D.H. Peregrine. "Steep unsteady water waves: An efficient computational scheme", *School of Mathematics Univ. of Bristol Report AM-84-04* (1984).

4. W.W. Schultz. *Proceedings of 11th IMACS World Congress* Vol. 2, Oslo. Norway (1985).

5. J.L. Hess. *Computer Method in Appl. Mechanics and Engineering 2*, 1 (1973).

6. J. Moran. *An Introduction to Theoretical and Computational Aerodynamics*, John Wiley & Sons (1983).

7. M.A. Kelmanson, *Computers & Fluids*, 11, 307 (1983).

8. G.R. Baker. D.I. Meiron and S.A. Orszag, *J. Fluid Mech. 123*, 477 (1982).

9. G. Golub, *Numerische Mathematik 7.* 206 (1965).

10. R. Fletcher and C.M. Reeves, *Computer Journal 7*, 149 (1964).

11. D.G. Dommermuth and D.K. Yue, *Proceedings of 16th ONR Symposium on Naval Hydrodynamics*, Berkeley, California (1986).

12. P. Grisvard, *Elliptic Problems in Non Smooth Domains*, Pitman Press (1985).

13. H.L.G. P̃. a, J.L.M. Fernandes and C.A. Brebbia, *Proceedings of the 3rd Int. Seminar on B.E.M.*, Irvine. California (1981).

14. W.M. Lin, J.N. Newman and D.K. Yue, *Proceedings of 15th ONR Symposium on Naval Hydrodynamics*, Hamburg, Germany (1984).

15. C. Patterson and M.A. Sheikh, "Regular boundary integral methods for stress analysis" in *Boundary Element Methods*. C.A. Brebbia, ed., Springer-Verlag (1981).

16. C.A. Brebbia and R. Butterfield, "Formal equivalence of direct and indirect boundary methods", *Appl. Math. Modelling 2*, 132 (1978).

17. G.R. Baker, "Generalized vortex methods for free-surface flows", in *Waves on Fluid Interfaces*, Academic Press. 53-81. (1983).

# LIST OF SYMBOLS

$E_2$           : root mean square error

$E_\infty$          : maximum error

e            : eccentricity of an ellipse ($\sqrt{a^2 - b^2}/a$)

              $a$ = long axis, $b$ = short axis

f            : desingularization parameter for locating kernel singular point

$I_k$           : part of contour integral near k th control point

L            : number of iteration of the matrix solver

$L_0$           : length of uniformly-spaced node

$L_e$           : length of distorted node

$N$            : number of total nodes

$N_s$           : number of kernel singularities on $R_s$

R            : domain of the problem

$R_s$           : radius of enclosing circular contour for desingularization

s            : curvilinear coordinate on contour

$U, V$         : row and column number of an overdetermined matrix

$x(s), y(s)$    : x and y coordinate of the contour

$z$            : complex coordinate of a point

$z_j$           : j th node

## Greek Letters

$\alpha$           : a constant (alpha)

$\beta$           : complex potential (beta)

$\beta_c$          : modified complex potential for corner problem

$\Gamma_{kj}$         : integral equation influence coefficient (upper case Gamma)

$\epsilon$           : parameter in a singular function (epsilon)

$\zeta_k$          : k th control point (zeta)

$\theta$           : tangent angle of the contour with positive x-axis (theta)

$\xi_c$          : corner node (xi)

$\phi$           : real part of $\beta$ (phi)

$\psi$           : imaginary part of $\beta$ (psi)

$\partial R_\phi$        : contour where $\phi$ is given

$\partial R_\psi$        : contour where $\psi$ is given

# LIST OF TABLES

# LIST OF FIGURES

Table I. Correlation Between Error and $Re(I_k^{(2)})$
(ellipse. inner problem. $\beta = \sin(z)$, $\phi$ given)

| eccentricity | weak | strong | overdetermined |
|:---:|:---:|:---:|:---:|
| 0.0 | 0.9997 | -0.9986 | 0.1915 |
| 0.6 | 0.9745 | -0.9711 | 0.3292 |
| 0.8 | 0.9075 | -0.8845 | 0.5856 |
| 0.9165 | 0.8367 | -0.7974 | 0.6133 |
| 0.9798 | 0.4809 | -0.7767 | 0.6451 |

**Table II.** $E_2$ Convergence Rates for Inner Problem
(ellipse. $\beta = \sin(z)$, $\phi$ given)

| e | system | $-LOG_{10}E_2$ | | | | conv. rate |
|---|---|---|---|---|---|---|
| | | N=32 | N=64 | N=128 | N=256 | |
| 0.0 | weak | 2.578 | 3.212 | 3.829 | 4.437 | 2.022 |
| | strong | 2.588 | 3.215 | 3.829 | 4.438 | 2.021 |
| | overdet. | 4.470 | 5.743 | 6.979 | 8.198 | 4.051 |
| 0.6 | weak | 2.732 | 3.366 | 3.982 | 4.590 | 2.022 |
| | strong | 2.743 | 3.370 | 3.984 | 4.592 | 2.020 |
| | overdet. | 4.646 | 5.399 | 5.997 | 6.598 | 1.993 |
| 0.8 | weak | 2.880 | 3.518 | 4.135 | 4.744 | 2.022 |
| | strong | 2.911 | 3.541 | 4.156 | 4.765 | 2.022 |
| | overdet. | 4.286 | 4.874 | 5.470 | 6.071 | 1.999 |
| 0.9165 | weak | 2.904 | 3.659 | 4.281 | 4.891 | 2.026 |
| | strong | 3.123 | 3.761 | 4.383 | 4.994 | 2.031 |
| | overdet. | 3.946 | 4.543 | 5.143 | 5.745 | 2.000 |
| 0.9798 | weak | 2.642 | 3.403 | 4.373 | 5.037 | 2.206 |
| | strong | 3.591 | 4.122 | 4.727 | 5.357 | 2.093 |
| | overdet. | 3.619 | 4.305 | 4.919 | 5.521 | 1.999 |
| 0.995 | weak | 2.684 | 3.249 | 4.104 | 4.737 | 2.103 |
| | strong | 3.926 | 4.547 | 5.092 | 5.630 | 1.805 |
| | overdet. | 3.578 | 4.215 | 4.864 | 5.489 | 2.079 |

Table III. $E_2$ Convergence Rates for Outer Problem
(ellipse. $\beta = 1/z$, $\phi$ is given)

| e | system | $-LOG_{10}E_2$ | | | conv. rate |
|---|---|---|---|---|---|
| | | N=32 | N=64 | N=128 | |
| 0.0 | weak | 2.3132 | 2.9299 | 3.5393 | 2.024 |
| | strong | 2.3162 | 2.9306 | 3.5395 | 2.023 |
| | overdet. | 4.7798 | 6.0105 | 7.2208 | 4.021 |
| 0.6 | weak | 2.2921 | 2.9161 | 3.5288 | 2.035 |
| | strong | 2.1563 | 2.7702 | 3.3789 | 2.022 |
| | overdet. | 3.6176 | 4.2079 | 4.7974 | 1.958 |
| 0.8660 | weak | 1.8871 | 2.5365 | 3.1584 | 2.066 |
| | strong | 1.8364 | 2.4573 | 3.0709 | 2.038 |
| | overdet. | 3.0694 | 3.7652 | 4.3682 | 2.003 |
| 0.9165 | weak | 1.6468 | 2.3176 | 2.9447 | 2.083 |
| | strong | 1.6530 | 2.2783 | 2.8956 | 2.051 |
| | overdet. | 2.6897 | 3.5067 | 4.1247 | 2.053 |
| 0.9798 | weak | 0.8131 | 1.5688 | 2.2367 | 2.219 |
| | strong | 0.9281 | 1.5898 | 2.2171 | 2.154 |
| | overdet. | 1.2885 | 2.6238 | 3.4247 | 2.661 |
| 0.9950 | weak | 0.5428 | 0.6898 | 1.4458 | 2.511 |
| | strong | 0.1215 | 0.8045 | 1.4655 | 2.196 |
| | overdet. | 0.2512 | 1.1748 | 2.5264 | 4.490 |

Table IV. $E_2$ for Various $N_s$, (N=16)

| $N_s$ | combined weak and strong | strong |
|---|---|---|
| 8 | -3.373 | - |
| 12 | -4.217 | - |
| 15 | -4.677 | - |
| 16 | -4.677 | -3.600 |
| 17 | -4.677 | -3.373 |
| 31 | - | -4.043 |
| 32 | -4.678 | -4.140 |
| 33 | - | -4.090 |
| 34 | - | -4.127 |
| 64 | - | -4.007 |
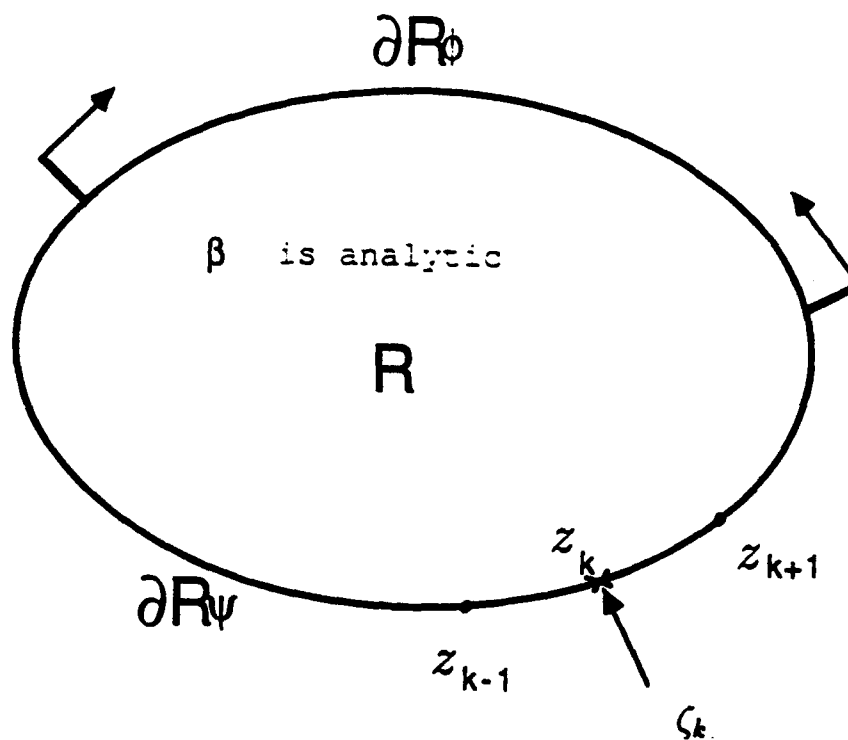
Figure 1: Domain and Bounding Surfaces
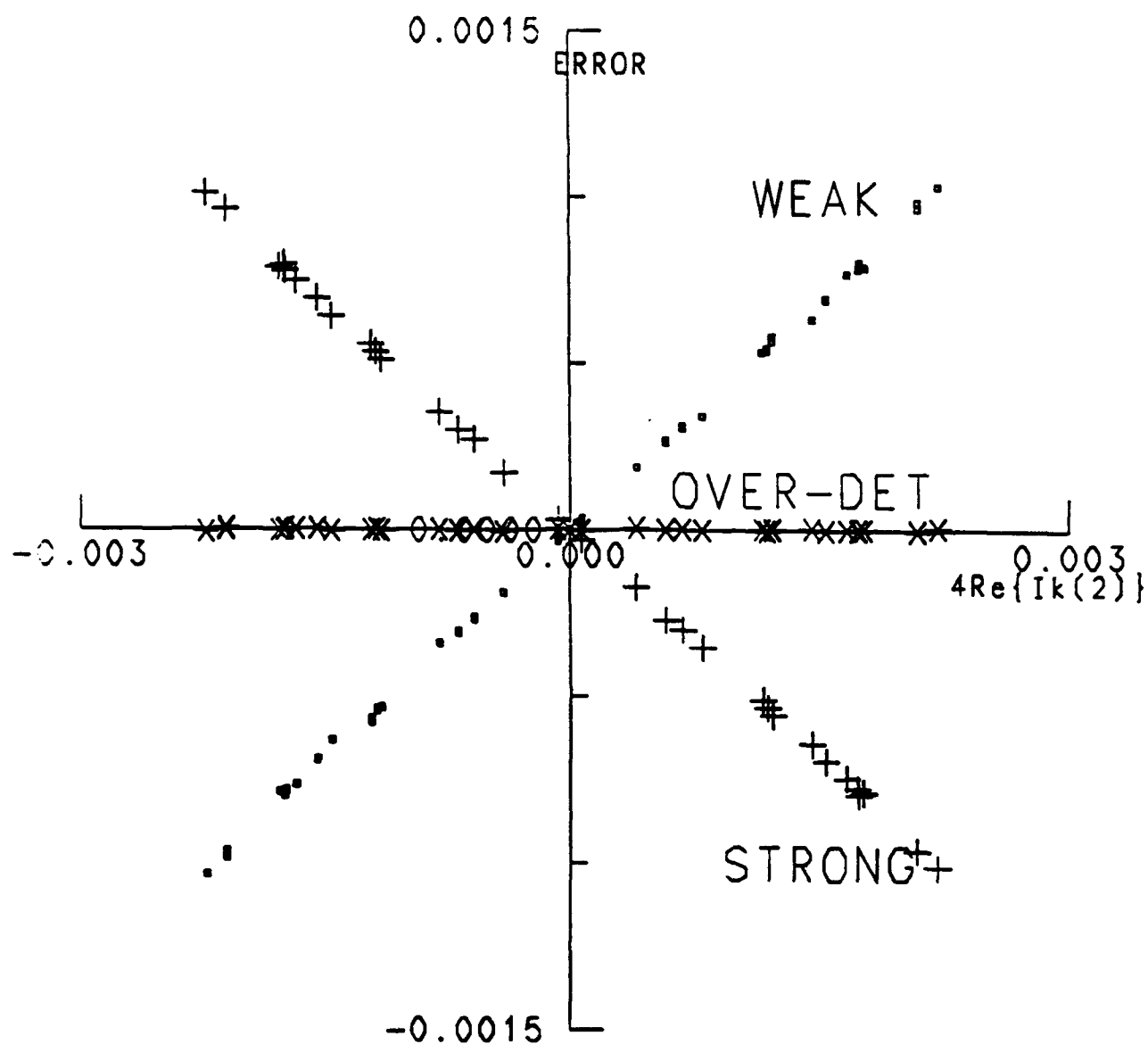
Figure 2: Correlations between Error and $I_k^{(2)}$
(circle, r=1, inner problem, $\beta = sin(z)$, $\acute{o}$ is given)
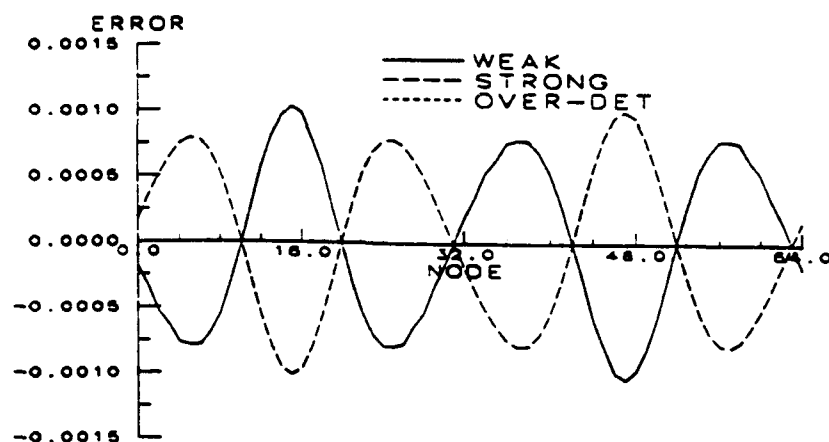
(a)   circle. r=1, inner problem. $\beta = sin(z)$, $\phi$ is given
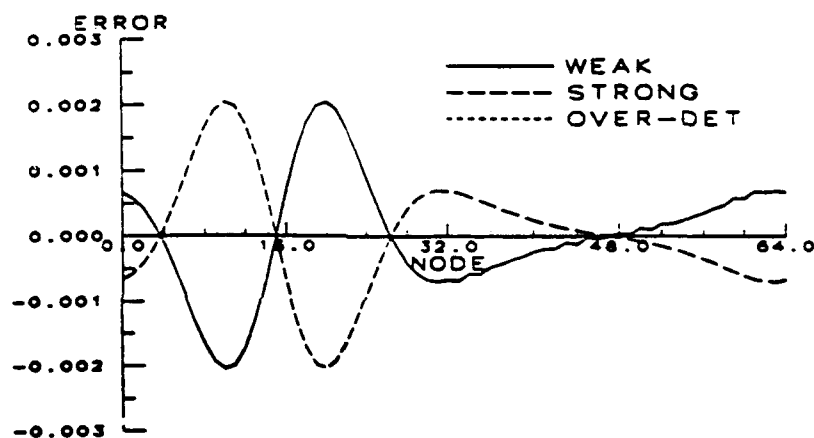


(b)   circle, r=1, inner problem, $\beta = e^{-iz}$, $\phi$ is given
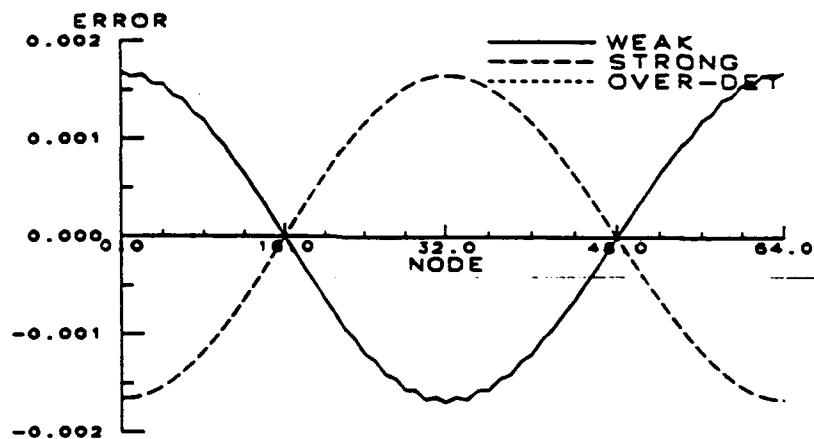


(c)   circle, r=1, outer problem. $\beta = z + \frac{1}{z}$, $\psi$ is given

Figure 3:   Error Distributions
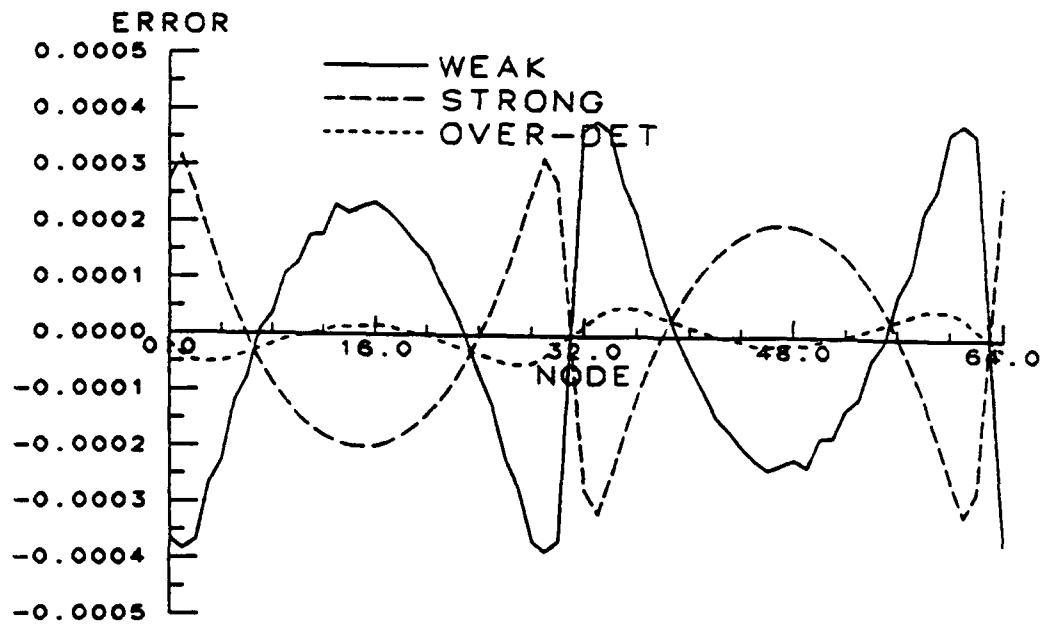
(a) Error Distributions
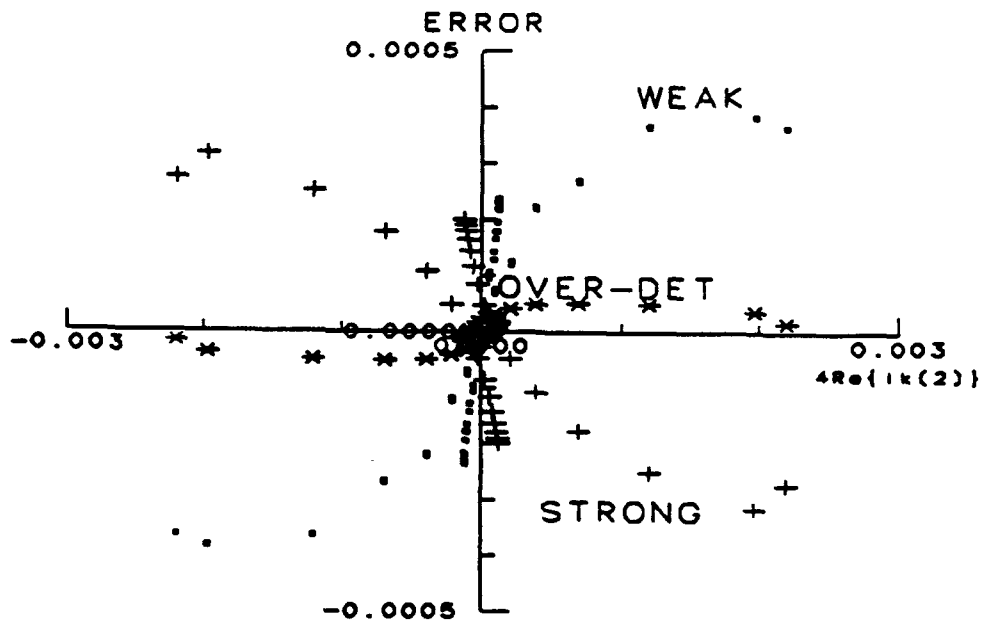


(b) Correlation Between Error and $I_k^{(2)}$

Figure 4:    Error Distribution and Correlations between Error and $I_k^{(2)}$
(ellipse. e=0.9165, inner problem. $\beta = \sin z$, $o$ is given
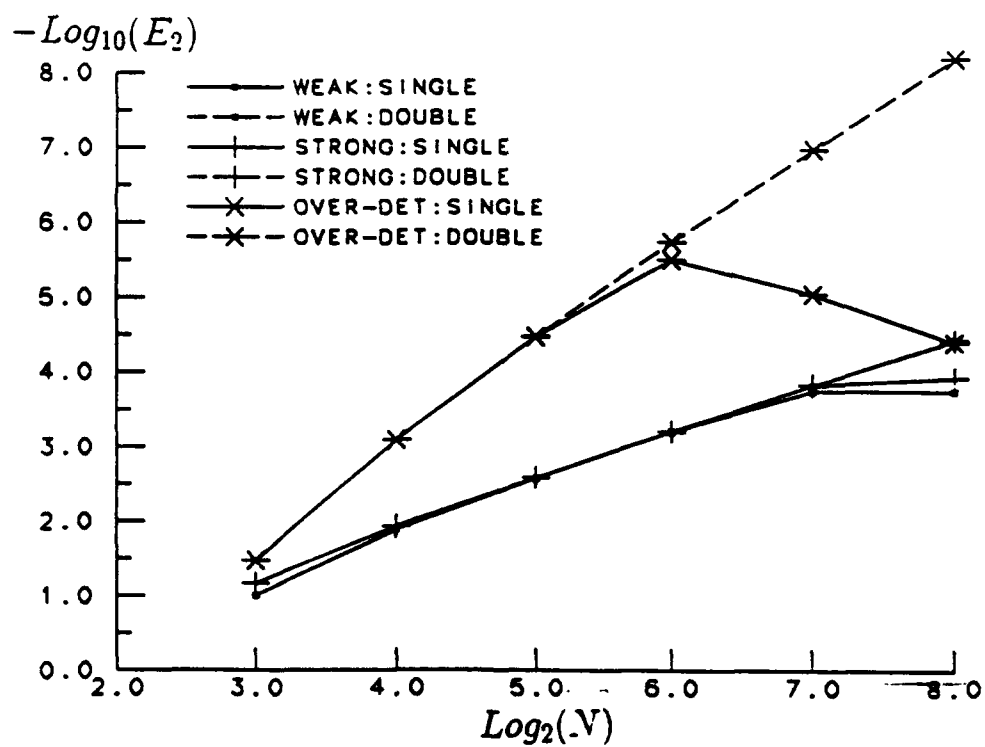
Figure 5: $E_2$ Errors for Various Number of Elements
(circle, r=1, inner problems,$\beta = sin(z)$, $o$ is given)
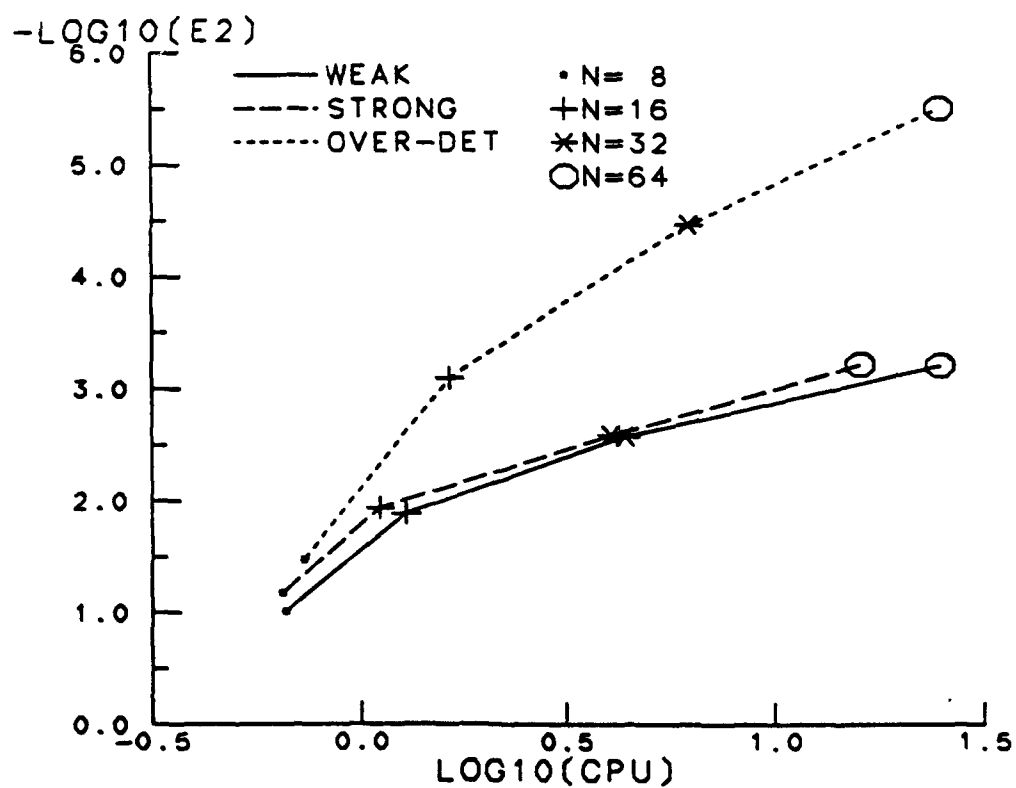
Figure 6: Relations between $E_2$ Errors and Computing Times
(circle, r=1, inner problems, $\beta = sin(z)$, $\phi$ is given)
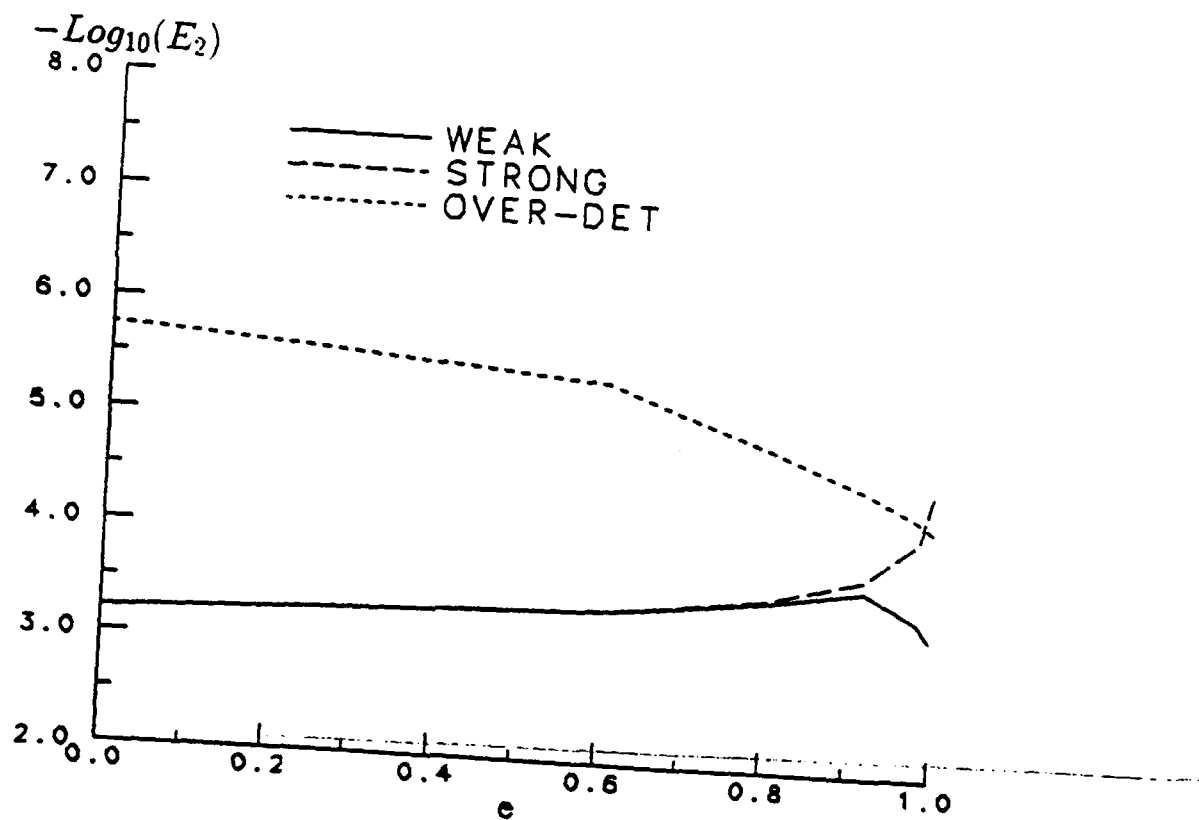
Figure 7: $E_2$ Errors for Various Ellipses
(N=64, inner problem, $\beta = sin(z)$, $\phi$ is given)
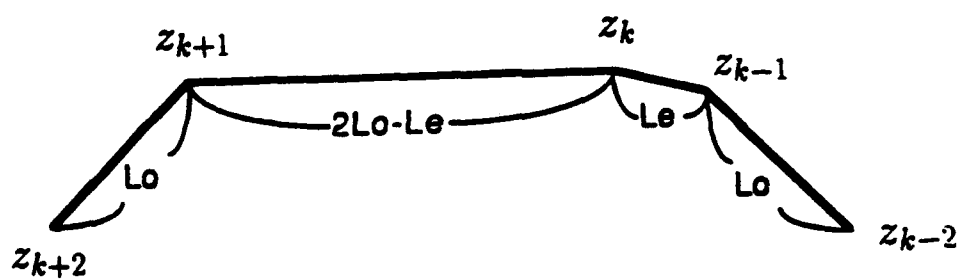
Figure 8: Non-uniformly Spaced Node
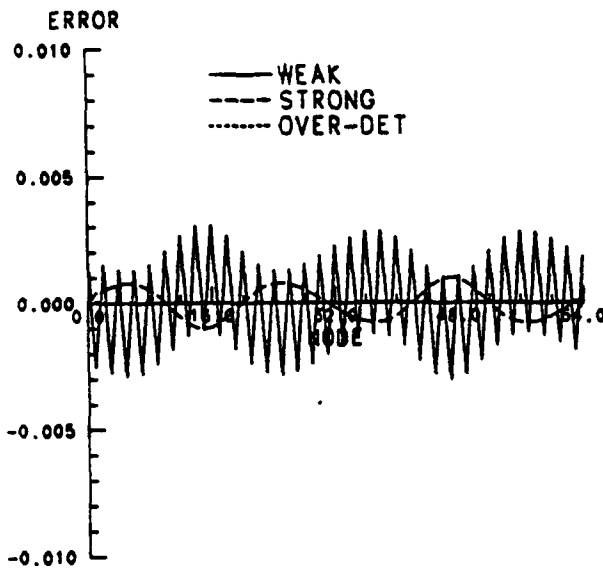
(a)  $L_e/L_0 = 0.9114$
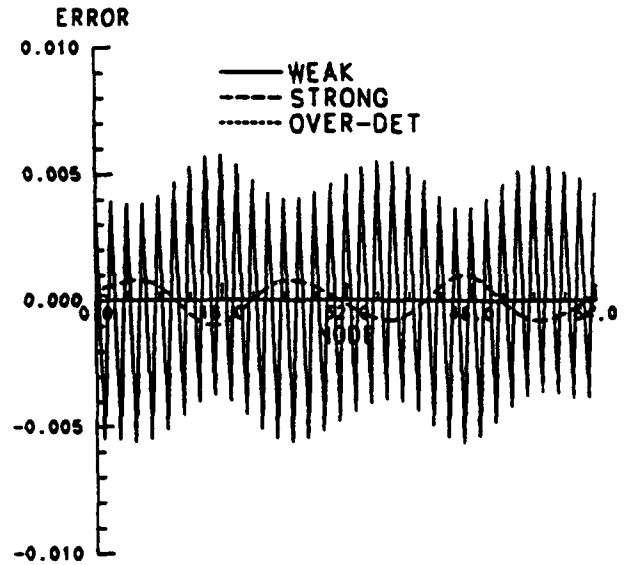
(b)  $L_e/L_0 = 0.7893$
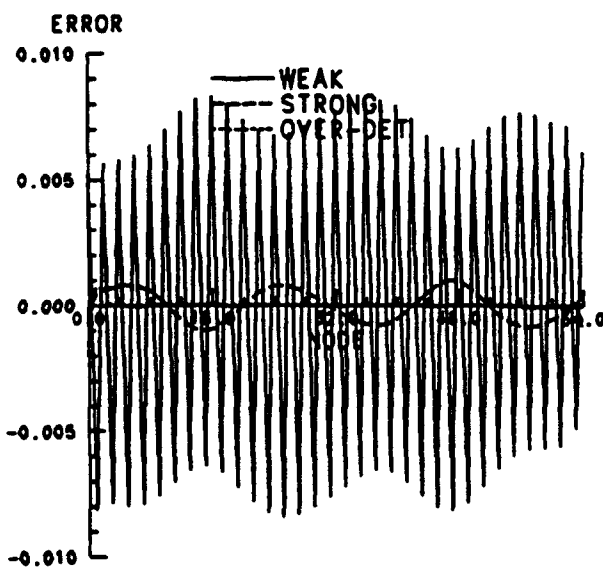
(c)  $L_e/L_0 = 0.6445$
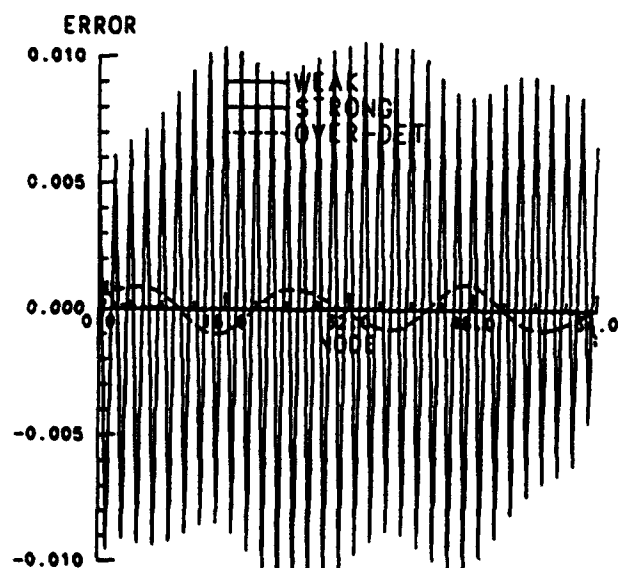
(d)  $L_e/L_0 = 0.4557$

Figure 9:  Error Distributions for Non-uniformly Spaced Node
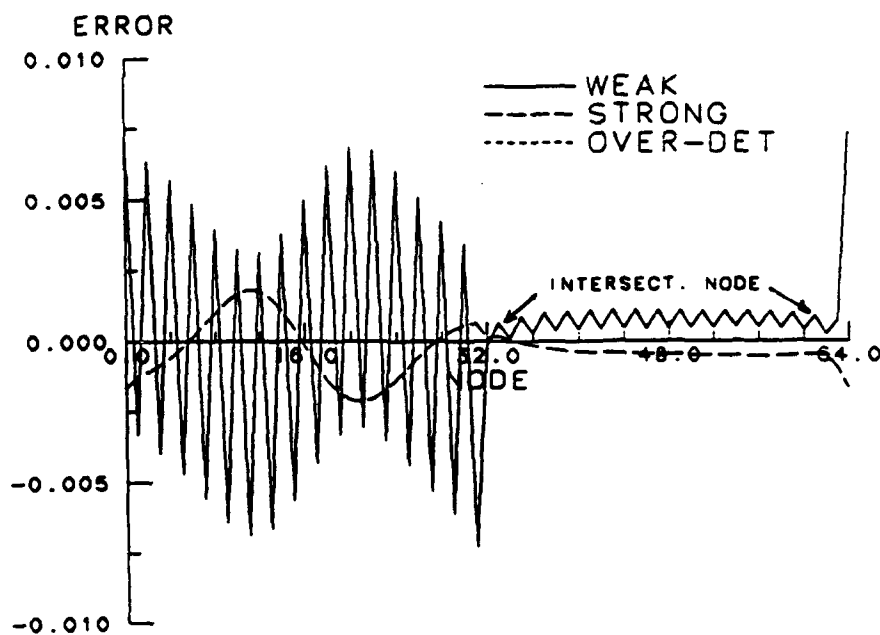
(a) CASE A
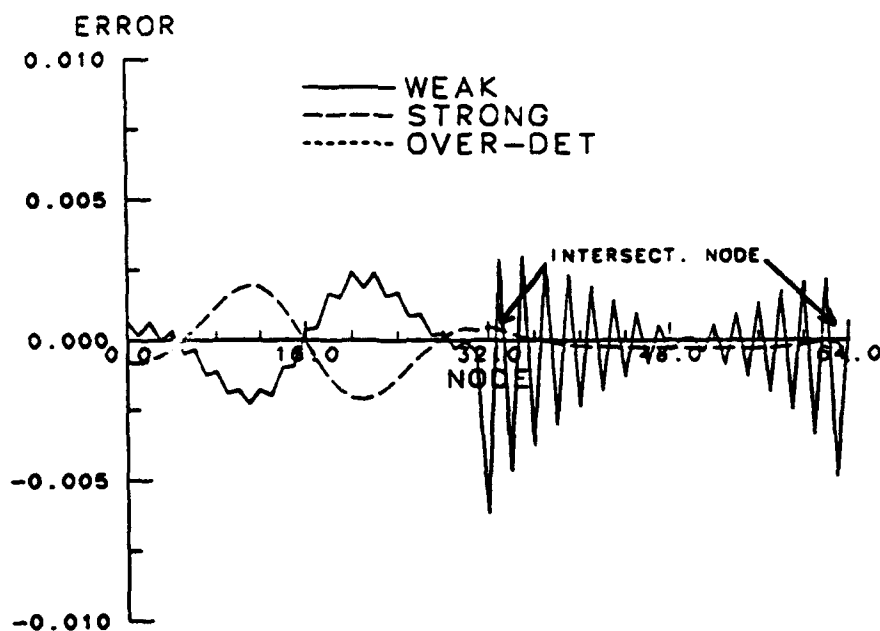
(b) CASE B

Figure 10: Error Distribution for a Mixed type Problem
(circle,inner problem, $\beta = e^{-iz}$)
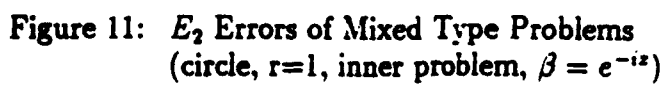
Figure 11: $E_2$ Errors of Mixed Type Problems
(circle, r=1, inner problem, $\beta = e^{-iz}$)
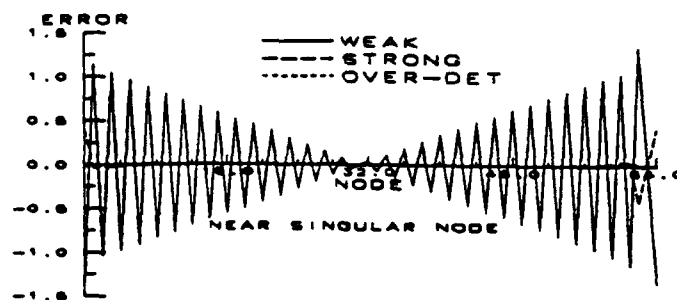
(a)  $\epsilon = 0.125$
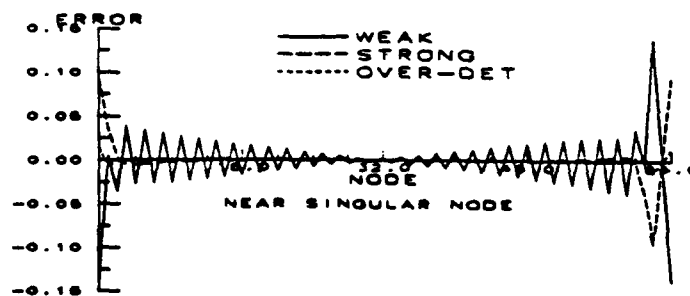


(b)  $\epsilon = 0.25$
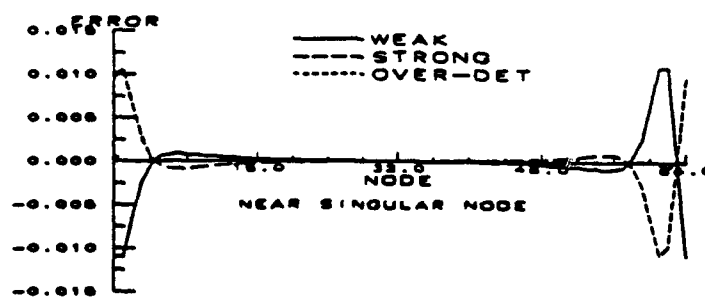


(c)  $\epsilon = 0.5$

Figure 12: Error Distributions for Singular Function Case
(circle, inner problem. $\phi$ is given)
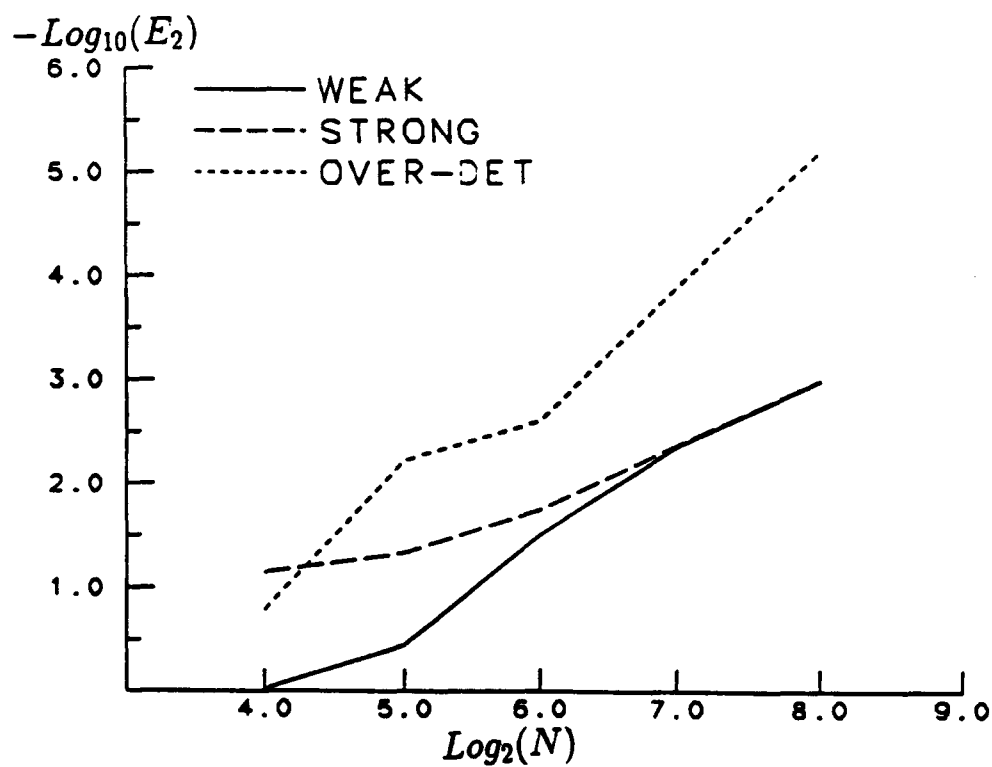
Figure 13: $E_2$ Errors for Singular Function Case
(circle, r=1, inner problem, $o$ is given. $\epsilon = 0.25$)
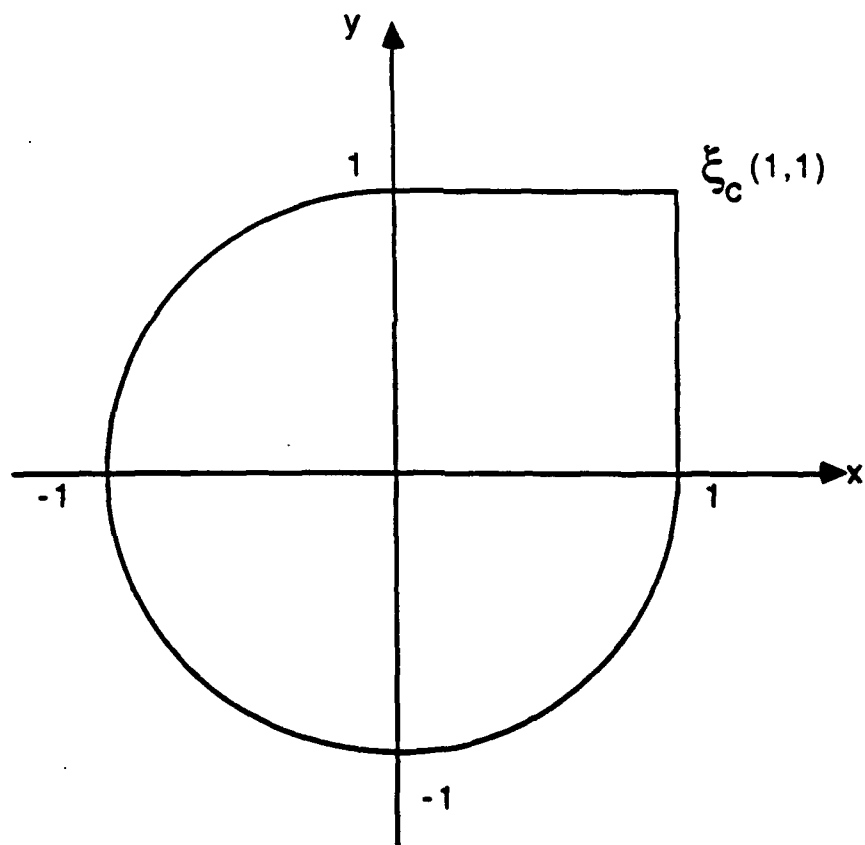
Figure 14: A Modified Circular Contour with a Corner
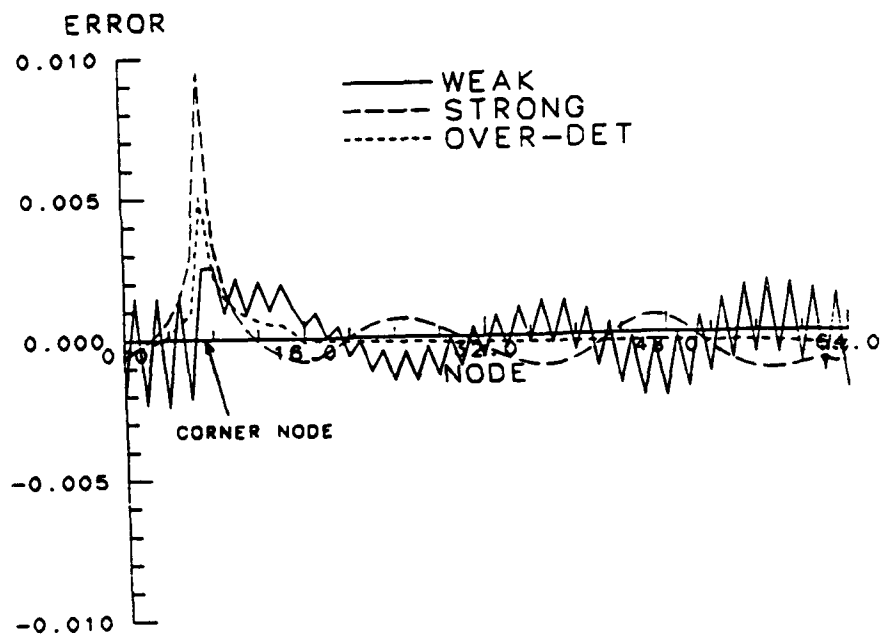
(a) Error Distribution. Unmodified
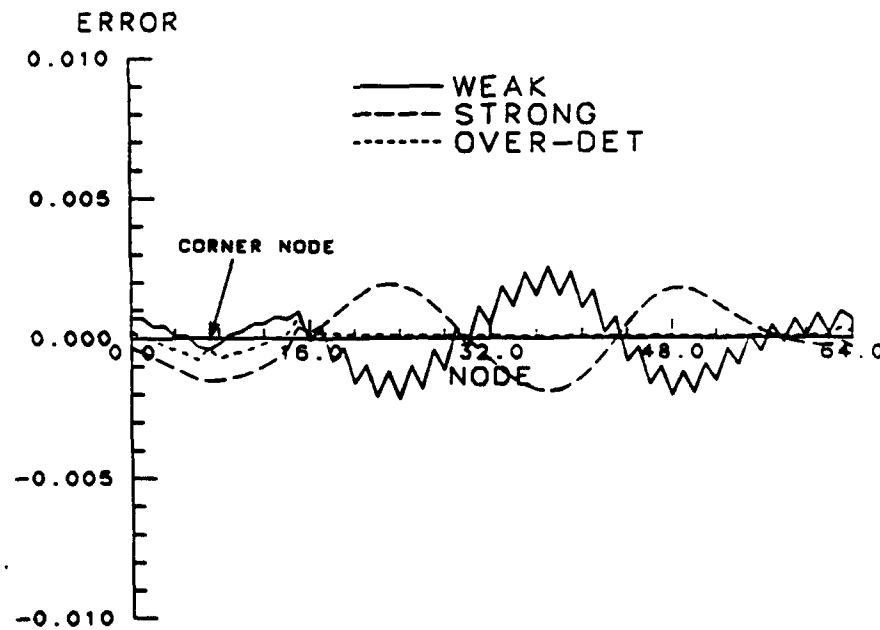


(b) Error Distribution, Modified

Figure 15: Error Distributions for a Corner Problem
(inner problem.$\beta = sin(z)$, $\varphi$ is given)
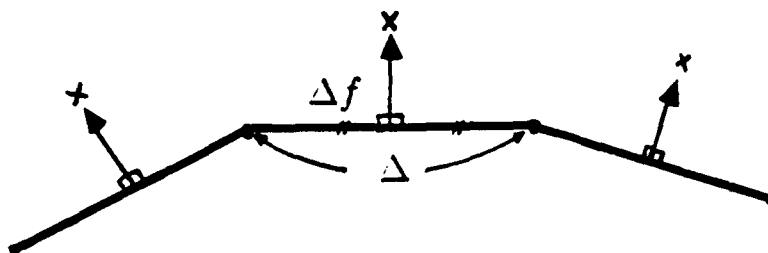
(a)    Strategy A
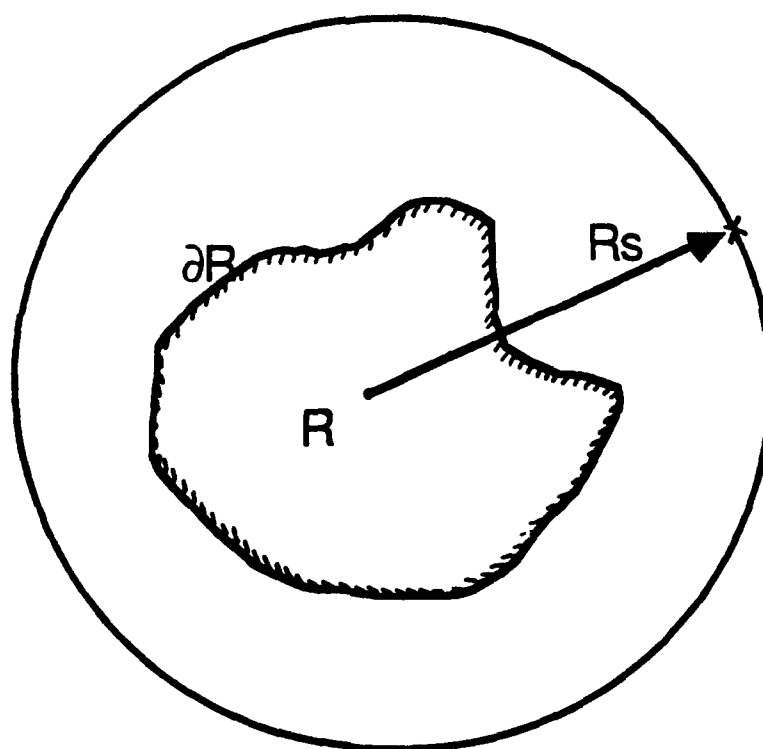


(b)    Strategy B

Figure 16: Location of Kernel Singular Points for Desingularization
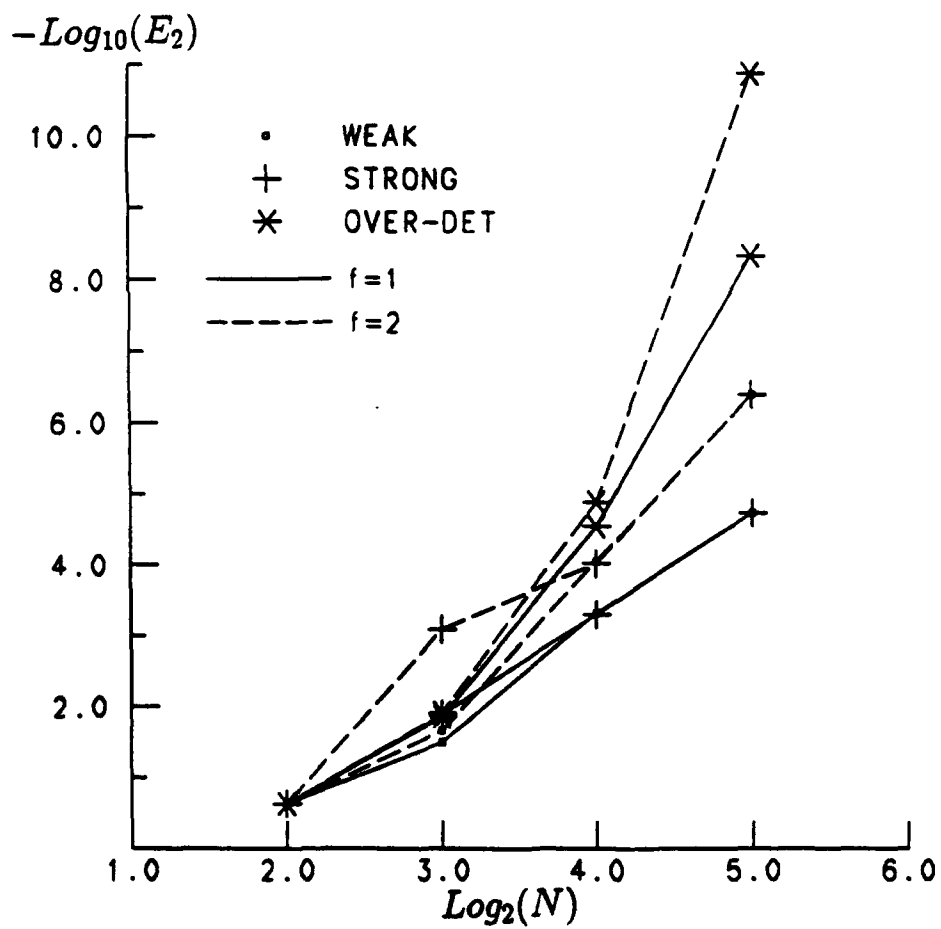
Figure 17: Convergence for Desingularized Boundary Integral Mehtod
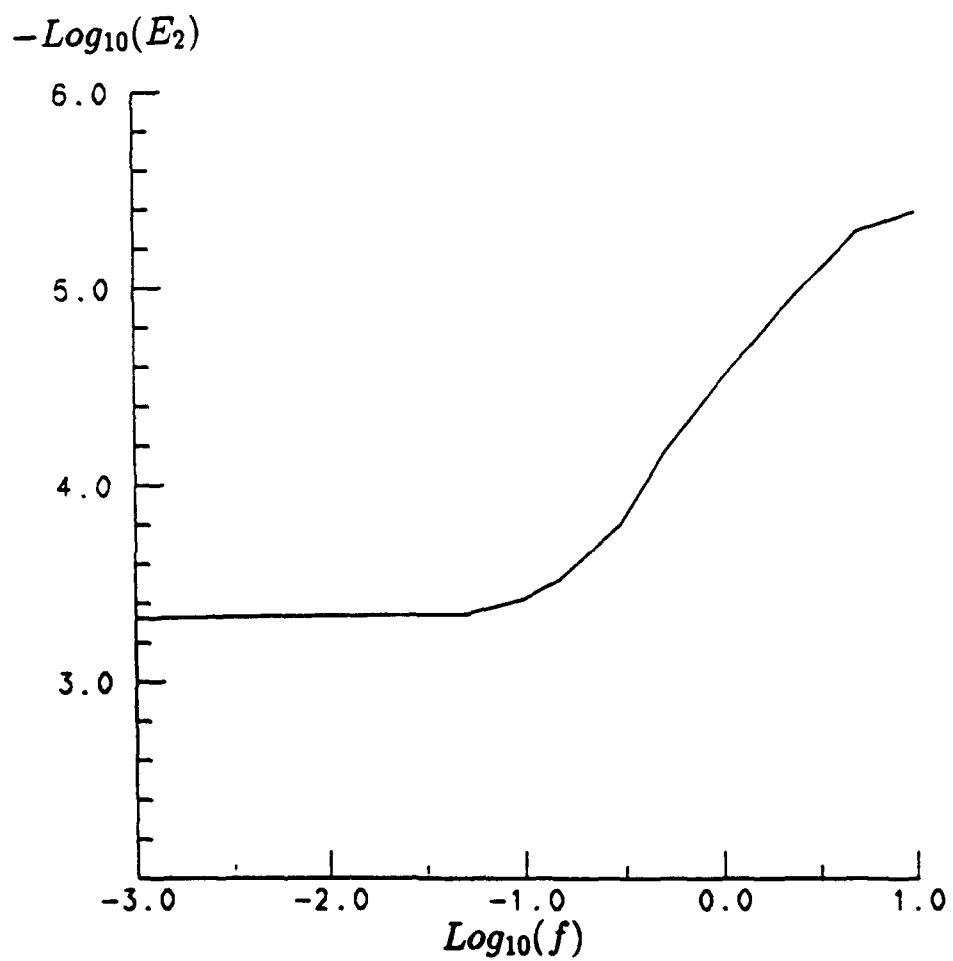
Figure 18: Effect of Desinglarization Parameter on Error
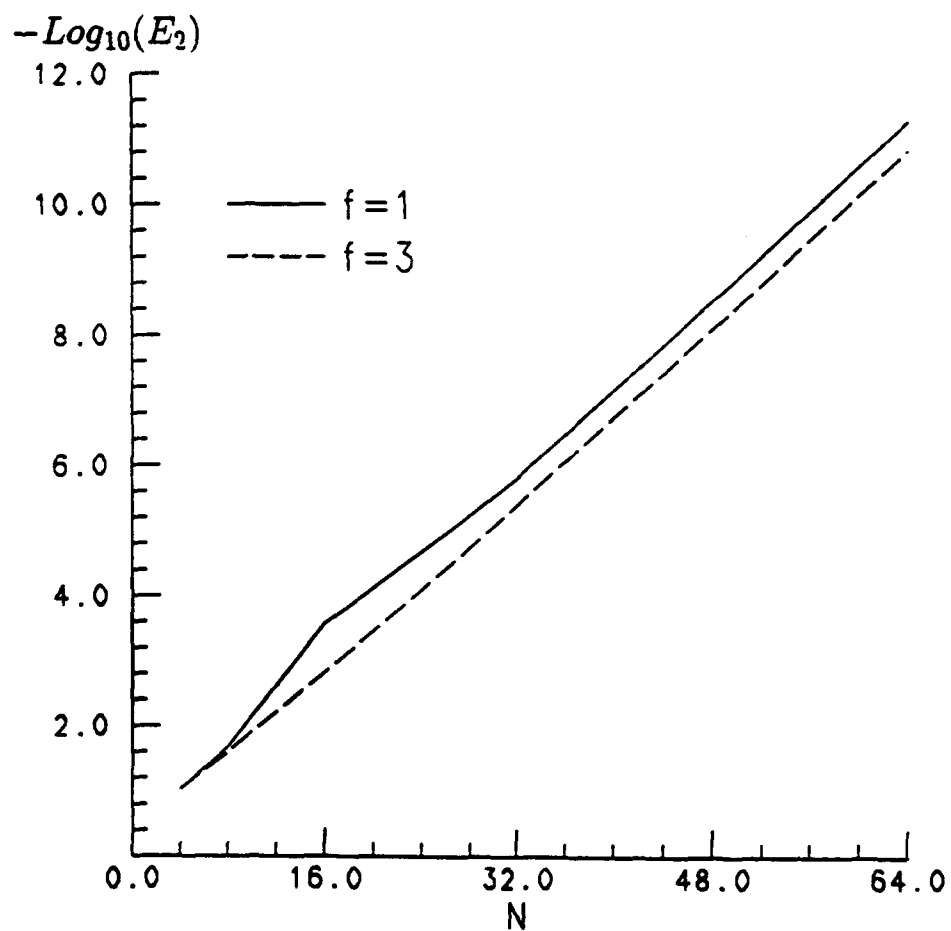
Figure 19:   Convergence for Nearly Singular Solution

$$(\beta(z) = 1/\{z - (1 + \epsilon)\}, \epsilon = 1.0)$$
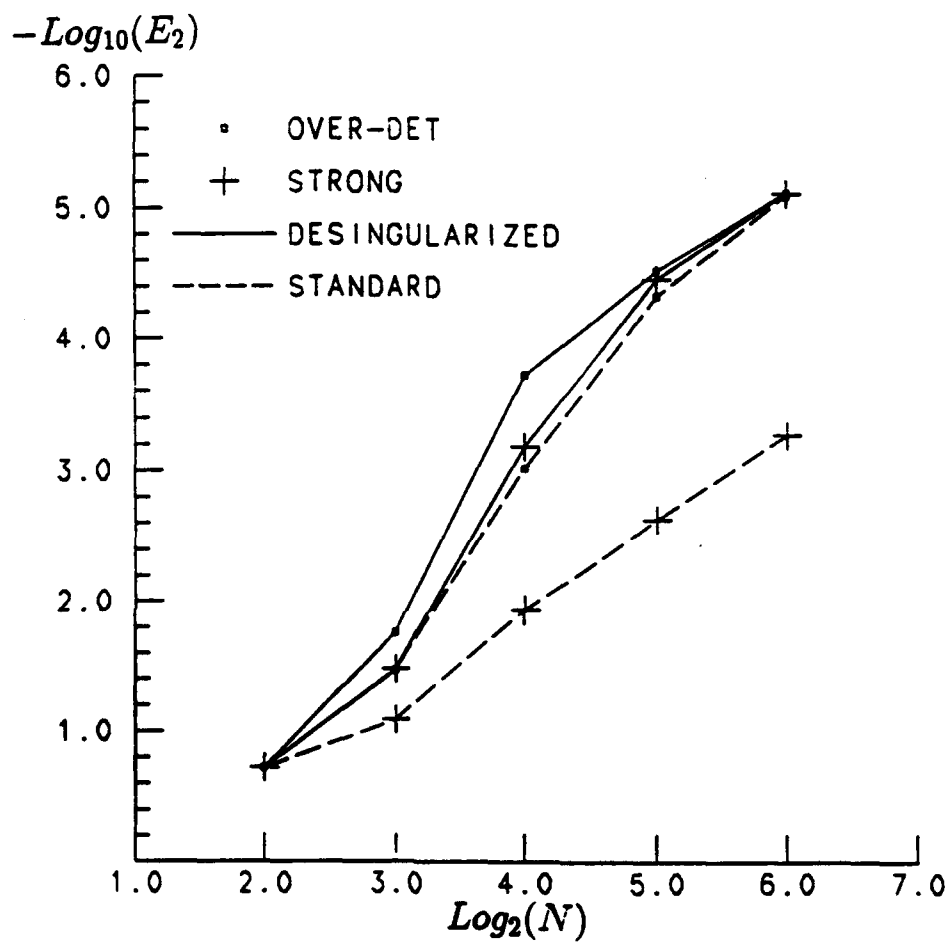
Figure 20: Comparison of Convergence

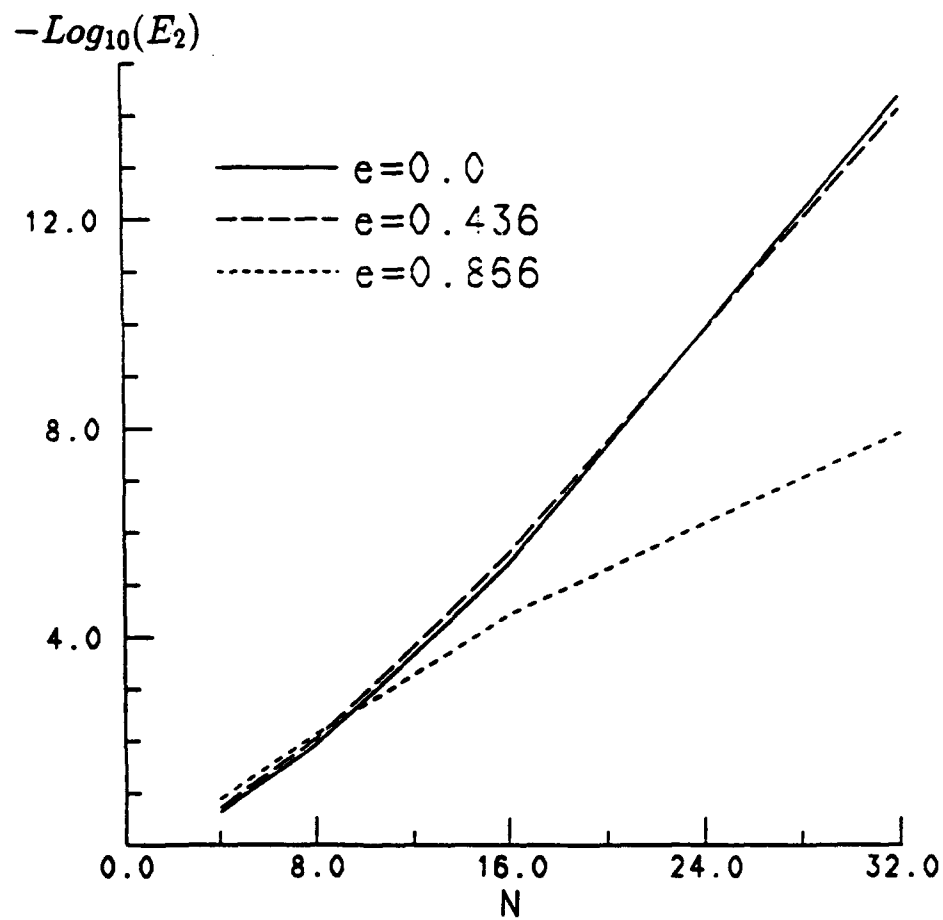(ellipse, $e = 0.436$, inner problem, $\phi$ is given, $f = 1$)

Figure 21: Convergence of Trapezoidal Method for nearly Circular Contours

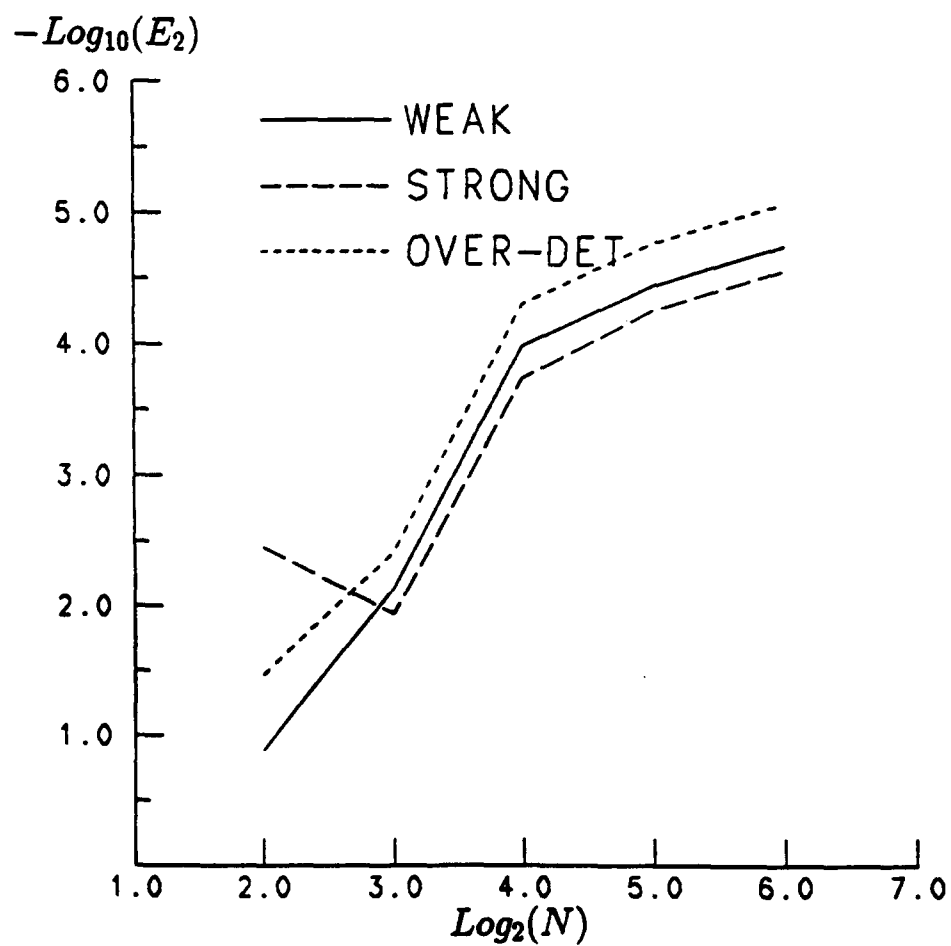(ellipses, inner problem, $\beta = \sin(z)$, $\phi$ is given)

Figure 22: Convergence of Trapezoidal Method for Unevenly Spaced Node Case
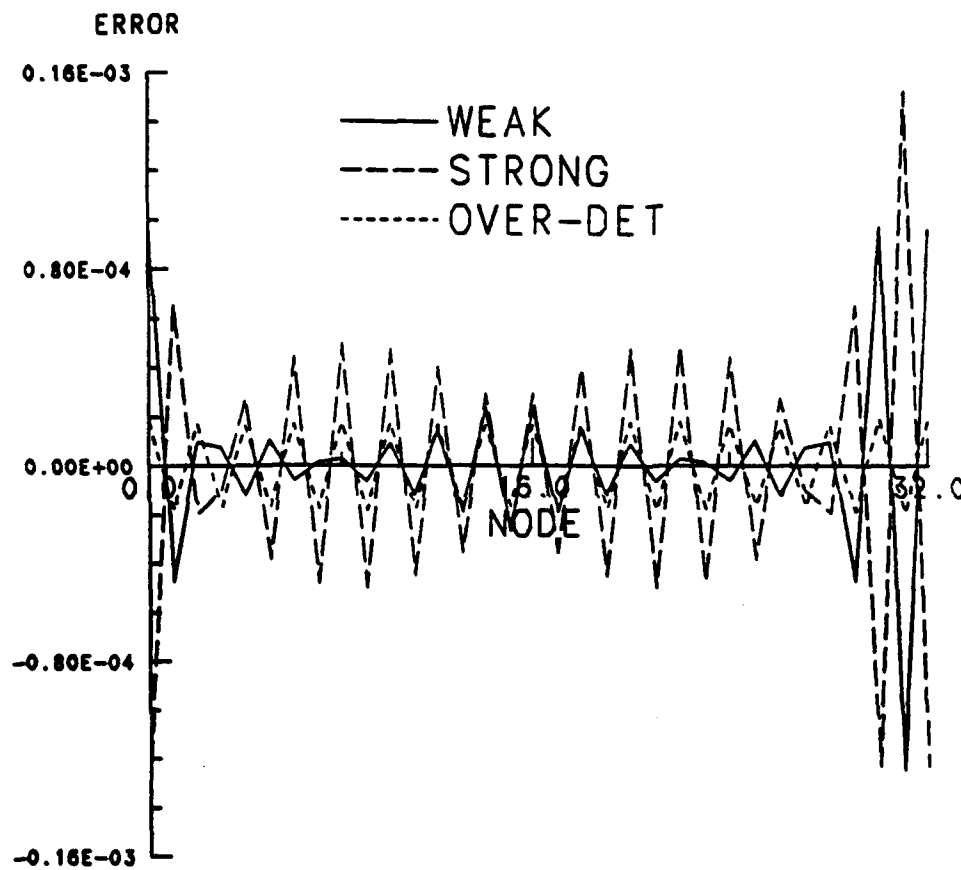
(ellipse, $e = 0.866$, $\beta = \sin(z)$)

Figure 23: Error Distribution of Trapezoidal Method for Unevenly Spaced Node Case
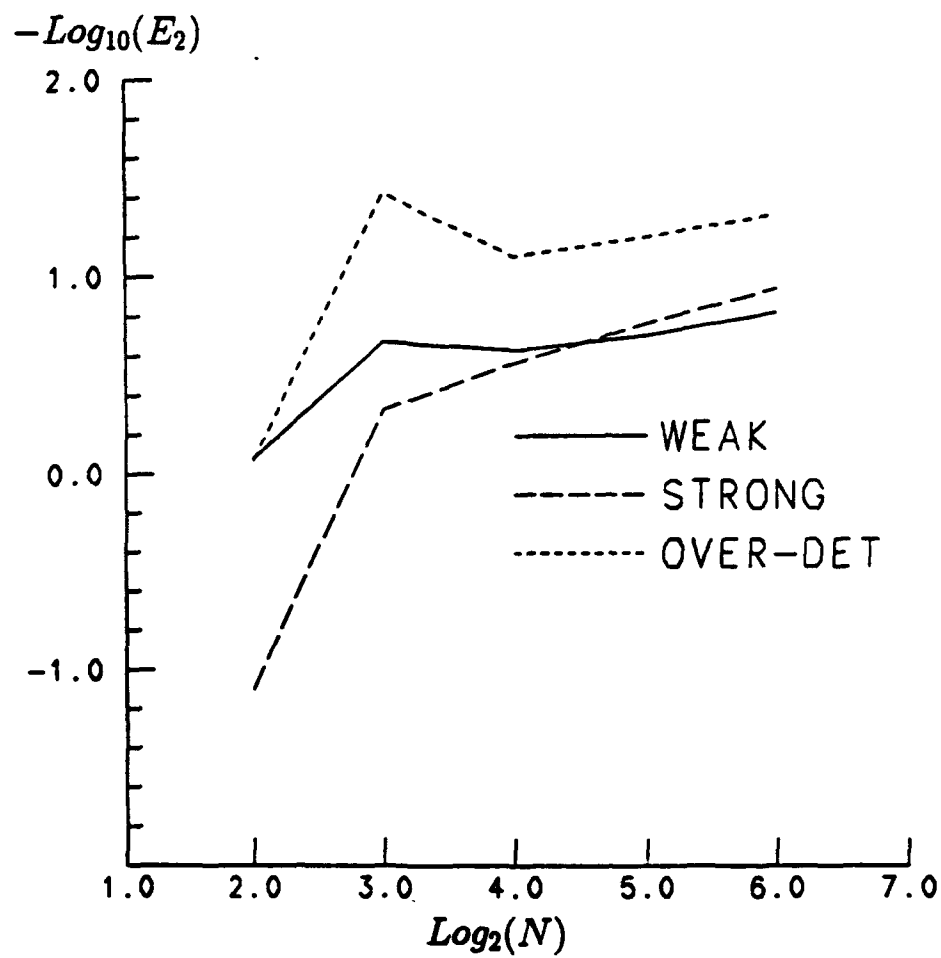
Figure 24: Error Distribution of Trapezoidal Method for a Square Contour

Ship Wake Consortium Agenda
Page Two

**Wednesday, October 5** - Room 134, NAME Department, North Campus

0830        Field and Laboratory Measurements of Surface Foam in Sea Water
               R.D. Peltzer, NRL; D.T. Rowley, UM

0915        Near Field Turbulent Ship Wake Computations
               M.B. Stewart, NRL

1000        Coffee Break

1015        Turbulent Ship Wake Predictions using SURFWAKE
               A.W. Troesch, UM; E.W. Miner, T.F. Swean, Jr., NRL

1045        Propeller Wake Measurements
               J. Blanton, S. Fish, DTRC

1145        Lunch

1300        Model Scale Free Surface Wake Measurements using DARTS
               A.W. Troesch, G.A. Meadows, L.A. Meadows, K.-P. Beier, UM

1345        PSH Laser-Doppler Anemometer Design
               W.W. Willmarth, UM

1415        Summary and Discussion

1445        Informal Demonstration at the Laser Flow-Visualization Facility
               L.P. Bernal, W.W. Willmarth, UM